Topical Review

Magnetization Dynamics in Artificial Spin Ice

S. Lendinez & M. B. Jungfleisch

Department of Physics and Astronomy, University of Delaware, Newark, Delaware 19716, USA

E-mail: mbj@udel.edu

July 9, 2019

Abstract. In this topical review, we present key results of studies on magnetization dynamics in artificial spin ice (ASI), which are arrays of magnetically interacting nanostructures. Recent experimental and theoretical progress in this emerging area, which is at the boundary between research on frustrated magnetism and high-frequency studies of artificially created nanomagnets, is reviewed. The exploration of ASI structures has revealed fascinating discoveries in correlated spin systems. Artificially created spin-ice lattices offer unique advantages as they allow for a control of the interactions between the elements by their geometric properties and arrangement. Magnonics, on the other hand, is a field that explores spin dynamics in the gigahertz frequency range in magnetic micro- and nanostructures. In this context, magnonic crystals are particularly important as they allow the modification of spin-wave properties and the observation of band gaps in the resonance spectra. Very recently, there has been considerable progress, experimentally and theoretically, in combining aspects of both fields – artificial spin ice and magnonics – enabling new functionalities in magnonic and spintronic applications using ASI, as well as providing a deeper understanding of geometrical frustration in the gigahertz range. Different approaches for the realization of ASI structures and their experimental characterization in the high-frequency range are described and the appropriate theoretical models and simulations are reviewed. Special attention is devoted to linking these findings to the quasi-static behavior of ASI and dynamic investigations in magnonics in an effort to bridge the gap between both areas further and to stimulate new research endeavors.

Frustrated magnetic systems such as spin-ice materials have been of scientific interest for a long time due to their highly degenerate ground states, which result in complex magnetic ordering and collective properties. The exploration of spin-ice systems started with crystalline materials such as the pyrochlores $Dy_2Ti_2O_7$, $Ho_2Ti_2O_7$, and $Ho_2Sn_2O_7$ [1, 2]. An interesting feature is that the fundamental excitations of these materials resemble the behavior of magnetic monopoles, which are connected by a "Dirac string" consisting of reversed dipole moments [3]. These emergent quasi particles were observed experimentally [4, 5, 6] shortly after the theoretical proposal by Castelnovo et al. [3]. Pioneering experiments on lithographically-defined arrays of interacting nanomagnets by Peter Schiffer's group demonstrated that similar physics can be explored in *artificial* spin ice (ASI), which opened the door to a new research field [7]. It was quickly realized that these artificially created spin-ice lattices offer unique opportunities to control and engineer the interactions between the elements by their geometric properties and arrangement [8, 9, 10]. This also means that the magnetization state is accessible through magnetic microscopy (such as scanning probe, electron, optical or x-ray microscopy). Analogous to their 3D counterpart, synthetically created ASI can also exhibit monopole and string excitations as shown theoretically by Mól et al. [11] and experimentally confirmed by Morgan et al. [12].

At the same time, the exploration of magnetization dynamics in magnetic nanostructures has flourished in the past decade and opened the field of magnonics [14, 15, 16, 17]. In essence, magnonics studies the behavior of spin waves (or their quasiparticles – magnons) in nano-structure elements. A prototypical magnonic device is a magnonic crystal with which the spin-wave properties can be modified leading to the observation of well-defined band gaps in the resonance spectra; e.g, [18, 19, 20, 21, 22, 23, 24]. From this end, harnessing the high-frequency response in ASI offers a rich playground for the investigation of how the (local) magnetization state of the ice and the presence of magnetic monopoles in the network affect the collective dynamics and vice versa [25]. Furthermore, ASI offers unique opportunities for the realization of re-configurable microwave oscillators in which the spectra depend on the micro-configuration of the array [26].

This topical review is structured in seven Sections. In Sec. 1, we introduce the concept of artificial spin ice and review magnetization dynamics and magnetotransport in nanostructures. Section 2 is devoted to the key fabrication methods that can be used to create ASI. Various different measurement methods and techniques to study artificial spin ices are discussed in Sec. 3. The magnetization dynamics theory and micromagnetics approach is explained in Sec. 4. Some of the most relevant recent experimental results on the dynamics of artificial spin ices from a magnonics perspective are presented in Sec. 5. In Sec. 6 we review recent developments in spin-transport related phenomena in ASI. Finally, in Sec. 7 we discuss challenges and possible future directions of the field.

1. Introduction

1.1. Water ice and artificial spin ice

Many of the interesting properties of water ice result from the hydrogen bonds between adjacent oxygen and hydrogen ions. Although it is a weak bond, it is critical for the structural properties of both water and ice. In water,

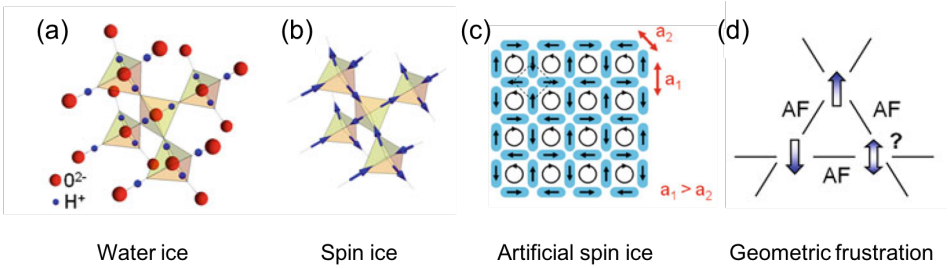

Figure 1. (a)Frustration in water ice where each oxygen has two protons closer and two protons further away from it. (b) Crystalline spin ice where two spins are pointing inwards and two spins are pointing outwards. (c) Ground state of square artificial spin ice. (d) Illustration of geometric frustration using the example of a triangular lattice with antiferromagnetic interactions. The third spin is frustrated since it can never simultaneously minimize the interaction energy with the other spins. Adapted from [13].

each oxygen atom is bonded to two hydrogen atoms. However, when water freezes it forms a tetragonal structure: Each oxygen atom in water ice is located at a vertex that has four nearest neighbor oxygen atoms, which are connected via a shared proton, as it is shown in Fig. 1(a) [8]. The proton is not in the middle between the two oxygen ions, but closer to one or the other [10]. This means that while the oxygen ions are periodically arranged, the location of the hydrogen ions is not [9]. The lowest energy state favors an arrangement that has two protons situated close to one given oxygen atom and two protons positioned close to a neighboring oxygen atom. This so-called *two in – two out* arrangement is known as the *ice rule* [8, 9, 13]. The ice-rule arrangement can be mapped to the spin system found for instance in pyrochlore materials such as $Tb_2Ti_2O_7$ and $Ho_2Ti_2O_7$ [1, 8, 27, 28], see Fig. 1(b), hence the name *spin ice*. The energies of the frustrated interactions between the rare-earth moments in these three dimensional spin ices are simultaneously minimized by having two magnetic moments point into and two point out of each tetrahedron [9], closely mimicking the behavior of water ice. There are six possible configurations for each tetrahedron that obey the ice rule and, therefore, the lowest energy state is macroscopically degenerate. At each given tetrahedron corner the ice rule is locally obeyed, but no long range order has been observed [9].

Advancements in modern nanofabrication and magnetic microscopy techniques in the past decade enabled the scientific community to artificially create spin-ice structures by patterning ferromagnetic thin films into 2D arrays of interacting nanomagnets [7, 29, 30], see Fig. 1(c). These artificial spin ice structures offer unique opportunities to control local and global interactions in the structures and to access the magnetization state of individual elements through various microscopy techniques such as scanning probe, electron, optical and x-ray microscopy. Some of these methods in the context of artificial spin ice will be discussed in detail below.

1.2. Frustration in ASI

Frustration arises in a physical system when all interaction energies cannot be simultaneously minimized, resulting in a finite value of the entropy even at 0 K temperature [8]. A model for geometrical frustration is a triangular lattice with antiferromagnetic interactions as shown in Fig. 1(d). In this simple example,

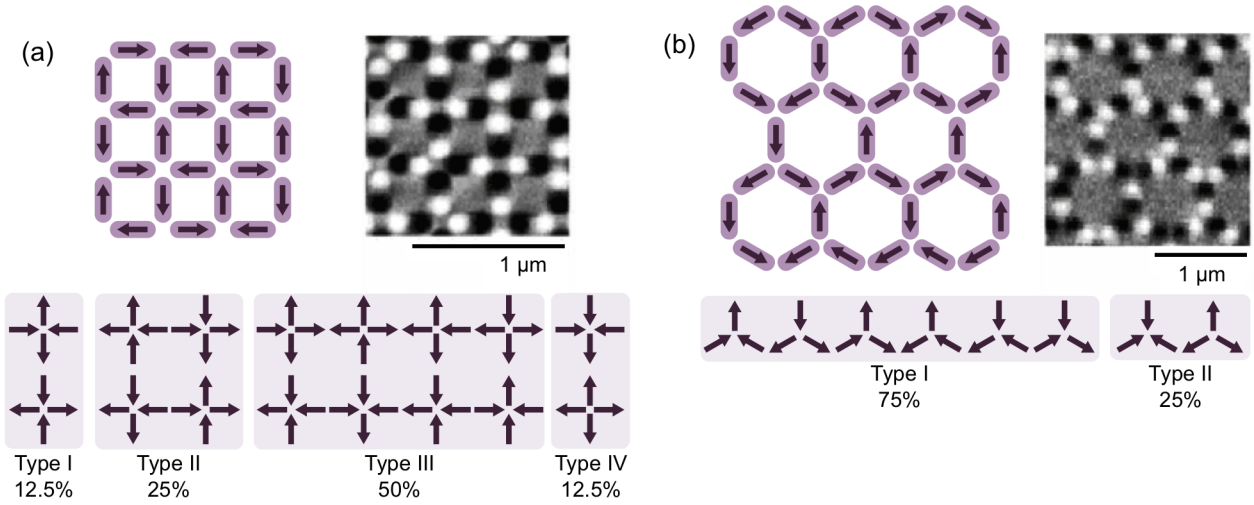

Figure 2. Schematics and magnetic force microscopy images of the spin configuration in two different types of ASI lattices: (a) Square lattice and (b) Kagome lattice. All possible orientations of the spins in a single vertex are shown, with their multiplicity in percentages. Adapted from [31].

the three antiferromagnetically coupled Ising spins can either point up or down. However, it is not possible to arrange them so that each pair is antiparallel [9]. Artificial spin ices are model systems to study frustrated interactions. They are composed of 2D arrays of magnetically soft nanomagnets, or *islands*, that have been patterned with an elongated shape to increase the anisotropy. To minimize the magnetic shape anisotropy energy, and since crystalline anisotropy is negligible in soft magnetic materials, the magnetization points in the direction of the long axis of the nanomagnets. Thus, each island behaves approximately as an Ising spin with two antiparallel states. Arranging the nanomagnets in specific lattice configurations may result in a geometrically frustrated structure, since the different interacting energies cannot all be minimized at the same time [32, 33, 34].

In the first experimental studies of ASI by Wang et al. [7], a square tiling was used to mimic the behavior of crystalline spin ice with spins in a two-in/two-out configuration, obeying the ice rule. In the square lattice, six out of the total of 16 configurations can be obtained that obey the ice rule. Figure 2(a) shows all possible orientations, grouped by energy level (type I, II, III, and IV). Dipolar interactions further separate the energy levels of the configurations in which the spins pointing in opposite directions are facing each other or orthogonal to each other (type I and II, respectively). Type III and IV are higher energy configurations. As the field gained interest, other creative lattices were invented with the goal to optimize the geometry to increase frustration; e.g., [30, 33, 34, 35, 36, 37, 38, 39, 40, 41, 42]. In a honeycomb or Kagome lattice, for instance, the ground state is sixfold degenerate [see Fig. 2(b)], and the system is fully geometrically frustrated.

Finding the ground state is hence of great interest to characterize the system's frustration. Considerable research efforts have been devoted in this regard. Since the individual islands' thermal energy barriers are on the order of 10^5 K [31] the system is "frozen" at room temperature, which allows the characterization of the state using

imaging techniques such as magnetic force microscopy or x-rays (see Sec. 3). In order to modify the state of these artificial spin ices, several methods have been used, such as demagnetization with external field protocols [29, 32, 43, 44, 45] or thermal activation [12, 36, 37, 46, 47, 48, 49].

1.3. Magnetization dynamics and magneto-transport in nanostructures

Magnetization dynamics and magnetoresistance in nanostructures are two of the most important topics in contemporary studies of magnetism, see e.g., [13]. With the ever increasing demand for faster and – at the same time – more efficient and scaled-down functional devices, a detailed understanding of the behavior and properties of magnetic materials confined to the nanoscale is both of fundamental interest and of particular importance for modern information technologies. To this end, the nonvolatility of magnetic materials has been – and continues to be – of paramount importance for data storage concepts. At the same time, the utilization of spin waves (or their elementary quanta – magnons) in nanostructures was envisioned as a means to process and transmit information decoupled from electric charge transfer [50]. Furthermore, magnonic architectures have been proposed as one of the "beyond-Moore" or "post-Moore" concepts by adding new functionalities to novel devices [51].

Various aspects of magnetoresistance in nanostructures have been studied in the past decades. Anisotropic magnetoresistance is the change in the electrical resistance due to different orientations of the magnetization. The electric field $\mathbf{E}$ created by the anisotropic magnetoresistance is:

$$\mathbf{E} = \rho_0 \mathbf{J} + \Delta\rho(\hat{\mathbf{m}} \cdot \mathbf{J})\hat{\mathbf{m}}, \tag{1}$$

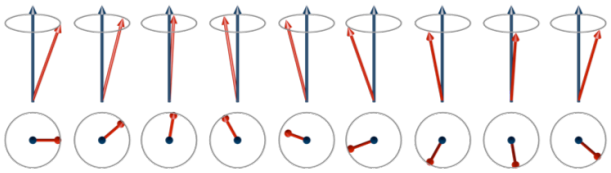

Figure 3. Illustration of the precession of spins about a magnetic field, creating a spin wave. Top: side view, bottom: top view.

where $\mathbf{J}$ is the electric current, $\hat{\mathbf{m}}$ is the unit vector of the magnetization, ρ_0 is the isotropic resistivity, and $\Delta\rho$ is the anisotropic magnetoresistivity. The first magneto-transport studies on artificial spin ice networks used a field-sweep measurement technique. It was demonstrated that anisotropic magnetoresistance (AMR) combined with nanowire reversal events were responsible for the observed sharp and abrupt changes in the resistance as a function of magnetic field [32, 52, 53]. Angular and field dependent investigations of the magnetoresistance in connected $Ni_{81}Fe_{19}$ nanowire networks revealed that the vertex regions mostly determines the anisotropic magnetoresistance in the networks [54, 55]. In certain geometries, magnetic field protocols can even place artificial spin ice networks in ordered ground states where the magnetoresistance is dramatically altered due to the order introduced within the vertex states [55].

Besides magnetic transport phenomena, the investigation of magnetization dynamics and spin waves are exciting topics in contemporary magnetism research. In the classical limit the precessional motion of the magnetization can be described by the Landau-Lifshitz-Gilbert equation [56]:

$$\frac{\mathrm{d}\mathbf{m}}{\mathrm{d}t} = -\gamma \mathbf{m} \times \mathbf{H}_{\mathrm{eff}} + \alpha \mathbf{m} \times \frac{\mathrm{d}\mathbf{m}}{\mathrm{d}t}, \tag{2}$$

with **m** the normalized magnetization, γ the gyromagnetic ratio, α the dimensionless Gilbert damping factor, and $\mathbf{H}_{\text{eff}}$ the effective field. Ferromagnetic resonance describes the uniform precession of the magnetization, while spin waves are the collective excitations of the spin lattice in a magnetically ordered solid, see Fig. 3. Analogous to quantizations of lattice vibrations known as phonons, magnons are the quasiparticles of spin waves [56].

From a dynamic perspective, characteristic length scales in magnonic devices are determined by the interaction between spins (exchange interaction on the short range and dipolar interactions on the long range) and can range from nanometers to micrometers [15]. The resonance frequency of spin waves is given by the saturation magnetization M_{S}, the spin-wave wavevector $\vec{k}$, the relative orientation between $\vec{k}$ and the magnetization $\vec{M}$, and the spin-wave stiffness D [15]. Typical spin-wave frequencies lie in the range between one and a few GHz [15, 16, 57]. The competition between exchange and dipolar interaction is responsible for an anisotropic spin-wave dispersion. In patterned magnetic media, the boundaries of the structures in combination with the anisotropic spin-wave propagation characteristics leads to fascinating properties. The research field of magnonics explores exactly this interplay between spin-wave confinement in one or two dimensions and anisotropic spin-wave dispersion. Some of the most important findings in this field are summarized in the following Section 1.4. For more detailed reviews of the field of magnonics, we refer to Refs. [14, 15, 16, 57].

1.4. Magnonic crystals

Various aspects of magnetic metamaterials have been discussed in the literature. From a dynamic perspective, magnonic crystals are particularly important since they allow for an unprecedented control of spin-wave properties [14, 15, 16, 57, 58]. Magnonic crystals are magnetic materials with a periodic modulation of magnetic parameters that leads to artificially created band structures.

Magnetic wires with a width of a few micrometers were studied by various techniques such as ferromagnetic resonance (FMR) [59], as well as optical techniques such as Brillouin light scattering (BLS) spectroscopy [60] and magneto-optical Kerr effect (MOKE) [61]. Due to the lateral constriction, spin-wave modes are localized either in the center or in the edge regions of the wire. The exact localization of the modes depends on the orientation of the magnetization with respect to the boundaries of the wire and the resonance frequency [15]. In general, the spin-wave wavevector k in a longitudinally magnetized wire is quantized across its width w, $k = \pi/w$, where w is the effective width of the wire that depends on dipolar pinning at the edges [15]. In a transversely magnetized wire, the demagnetizing field reduces the internal magnetic field creating a *spin-wave well* that channels spin waves along the edge of the wire [60]. This mode is hence called edge mode.

The first magnonic crystals studied were one dimensional arrays of densely packed magnetic wires made of permalloy and yttrium iron garnet, where the formation of well-defined bandgaps was observed [19, 62]. Although spin waves are defined only inside a magnetic medium, a coherent collective excitation can exist in isolated magnetic wires due to long-range dipolar coupling [15].

Furthermore, magnetic antidot lattices were extensively studied in the past decade; e.g., [63, 64, 65, 66, 67]. Antidot lattices are periodic arrays of holes patterned in a

magnetic thin film and are essentially two-dimensional magnonic crystals. In these two-dimensional structures localization effects are particularly important: spin-wave modes can either be localized or extended in the magnonic crystal. The internal magnetic field plays a major role here: it was shown that high frequency modes typically have their maxima between the antidots, whereas low-frequency modes are found to have the highest amplitude next to the antidots mimicking the areas of a reduced internal field [15, 16]. More recently, the reprogrammability of magnonic band structures was studied in layered magnonic crystals and nanowire arrays [68].

2. Fabrication methods

Typically, artificial spin-ice structures have lateral dimensions below the micrometer range, which requires the use of state-of-the-art nanofabrication techniques. Various approaches can been used depending on the details of the desired device. The need of nanometer sizes in artificial spin-ice networks is twofold. In order to have Ising-like spins, the magnetization should behave as a single domain spin in each island, which is achieved by patterning elongated islands at the nanoscale. Moreover, since the predominant order is short-ranged, small gaps between islands are preferred to optimize nearest-neighbor interactions. In the following, the main methods for the fabrication of ASI networks are reviewed.

An overview of the different lithographic processes is shown in Fig. 4(a)-(d). Fabrication most commonly involves coating a substrate with a sensitive resist, which is then exposed to transfer the desired pattern. After exposure, the resist is developed and depending on the resist composition, the exposed areas will be removed [positive resist, left column in Fig. 4(c)] or stay [negative resist, right column in Fig. 4(c)]. In most of the works on ASI, positive resists were used. In this case, the magnetic material – typically permalloy ($Ni_{80}Fe_{20}$, Py) – is deposited afterwards and the resist finally lift-off processed, which results in the magnetic material remaining in the exposed areas, see Fig. 4(c). An example of a square lattice spin ice obtained with this method is shown in Fig. 4(e).

Modern optical lithography techniques achieve minimum feature sizes of approximately 1 μm, which is too large for the fabrication of ASI. Due to its high resolution, the standard method for the fabrication of small arrays of nanomagnets, and ASI in particular, is electron beam lithography. An additional advantage of electron beam lithography is its relatively easy processing and adaptability. On the flip side, electron beam lithography is slow and expensive compared to optical lithography, and hence not suitable for the fabrication of large arrays, which precludes it as an industrial-scale fabrication method. To minimize the time for fabrication and the associated costs, a complete device that consists of the ASI structure and other larger device parts such as *dc* leads or antennas is usually fabricated by combining different lithographic techniques.

The typical electron beam lithography process is as follows [see Fig. 4(c)]. A bilayer resist is spin coated on a silicon wafer. The pattern is then written with the electron beam scanning over the sample exposing the resist. A solvent is used after exposure to remove the exposed parts of the resist stack. A thin layer of magnetic material (below 50 nm) is deposited and the resist finally removed with another solver.

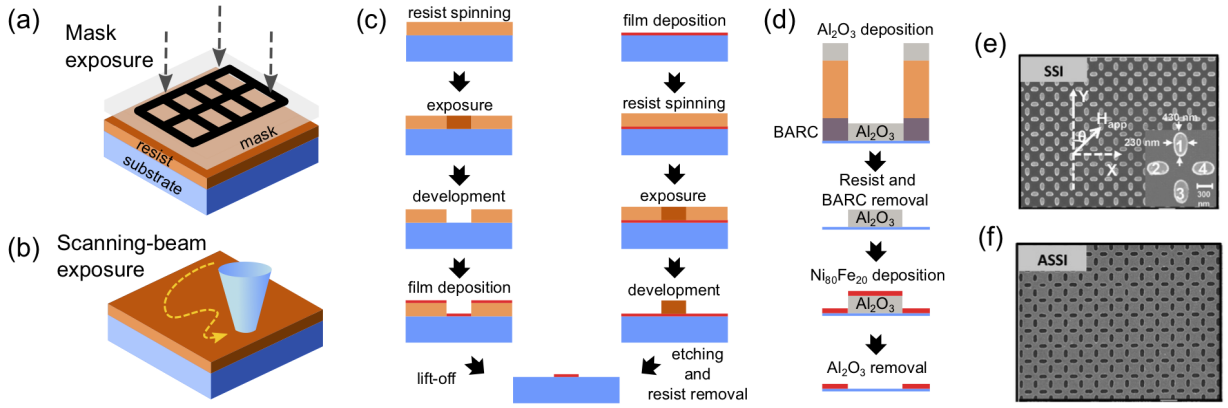

Figure 4. Summary of the main differences between lithographic processes used in the fabrication of ASIs. (a) Typical optical lithography techniques shine light on the photoresist through a mask. A single exposure covers an extended area. (b) Techniques such as electron beam lithography scan the beam over a sensitive resist. They present the advantage of an easier design-to-device implementation at the cost of speed. (c) Comparison of the positive and negative lithographic processes. (d) An alternative way of obtaining a reversed structure with a positive photoresist. (e) Scanning electron microscopy images of a square spin ice lattice (SSI) fabricated with the typical positive-tone process and (f) an anti-square spin ice (ASSI) lattice fabricated with the process illustrated in (d). Figs. (d), (e) and (f) adapted from [69].

A variety of bilayer resist stacks have been used for the fabrication of ASIs with a positive electron beam lithography process, such as polymethylglutarimide (PMGI) for the bottom layer and polymethyl methacrylate (PMMA) for the top layer [7, 70], or different compositions of PMMA [41]. Even a single-layer resist of ZEP can be used to successfully transfer the pattern via lift-off [71, 72]. It was also shown that a negative lithography process using ma-N or hydrogen silsesquioxane (HSQ) can be used [29]. In this case, only the electron-sensitive exposed resist remains on the substrate, see right column of Fig. 4(c). The transfer of the pattern typically occurs through etching of the previously deposited material. This technique has the advantage of a smaller achievable size; however, the remaining resist is harder to remove and usually an oxygen plasma step is necessary for the removal. In some cases, this might not be suitable for the process as it might damage other device parts.

Another technique that has been used for the fabrication of ASI is focused ion beam [73]. Here, the focused ion beam mills the magnetic film by bombarding the surface with ions, directly transferring the pattern without the need of a resist.

Both electron beam lithography and focus ion beam are inherently slow since they require a beam to be scanned over the sample, Fig. 4(b). The advantage of optical lithography techniques is that large areas can be exposed simultaneously and the pattern is transferred to the photosensitive resist via a mask, see Fig. 4(a). Optical lithography is typically fast, but the resolution is limited to the micron scale due to the relatively large wavelength. In general, this renders standard optical lithography as not suitable for the fabrication of ASI. To circumvent this problem, however, light with a smaller wavelength can be used. It was shown that using deep-ultraviolet optical lithography (DUV) at 193 nm, large areas

of nanostructures can indeed be fabricated [69], see also Fig. 4(a). Figure 4(e) shows a scanning electron microscopy image of a square spin ice (SSI) lattice. In addition, Zhou et al. used a combination of lift-off and etching to pattern anti-ASIs [74, 75], consisting of extended thin films in which the lattice structure is removed [see Fig. 4(d)]. For this purpose, a photoresist was first spinned and the lattice pattern exposed using DUV. Afterwards, Al_2O_3 was deposited and the resist lift-off. The $Ni_{80}Fe_{20}$ film was then deposited and the Al_2O_3 removed, which resulted in the pattern of the anti-square spin ice (ASSI), see Fig. 4(f).

3. Measurement techniques

Traditionally, a variety of different complementary experimental techniques is used in magnonics: microwave-based techniques such as ferromagentic resonance and spin-wave spectroscopy, optical techniques such as magnetic optical Kerr effect microscopy and Brillouin light scattering, as well as pump-probe techniques with femtosecond lasers and x-ray microscopy have been applied [14, 15, 16, 57]. Each technique has its own advantages, as will be laid out in the rest of this section. Not all of those techniques have been used to explore magnetization dynamics in artificial spin ice yet, but they could potentially be exploited to understand underlying mechanisms. In the following, the main experimental methods used to characterize dynamics in artificial spin ice are reviewed.

3.1. Magnetic transport measurements

Transport measurements have been used for many years to determine the direction of the magnetization with respect to the applied electric current. The change in resistance as a function of magnetic field can be due to different effects – anisotropic magnetoresistance (AMR) [76], spin Hall magnetoresistance (SMR) [77], giant magnetoresistance (GMR) [78], etc. – and give information about the underlying magnetic properties of the sample.

Modern fabrication techniques allow precise patterning of contacts in different regions of the sample. In this way, it is possible to perform precise voltage measurements in different orientations and locations with respect to the applied current.

Since all magnetic transport measurements on ASIs reported to date have exclusively employed AMR effects, we present here a short review of AMR in magnetic metals. AMR can be written as:

$$\rho = \rho_0 + (\rho_\parallel - \rho_\perp)(\mathbf{j}\cdot\mathbf{m})^2 = \rho_\perp + (\rho_\parallel - \rho_\perp)cos^2\theta, \quad (3)$$

with ρ_0 the average resistivity, $\rho_\perp$ the perpendicular resistivity, $\rho_\parallel$ the longitudinal resistivity, $\mathbf{j}$ the current density vector, $\mathbf{m}$ the unit vector pointing in the magnetization direction, and θ the angle between $\mathbf{j}$ and $\mathbf{m}$. In other words, the highest resistance value is observed when the magnetization is parallel to the current direction ($\theta = 0°$), while the lowest resistance values occur when the two directions are perpendicular to each other ($\theta = 90°$). For instance, steps in the AMR are indication of island switching in square-network ASI [54, 79], as the relative angle between the applied current and the magnetization momentarily changes.

Another magnetoresistance effect that could potentially be used for studies on artificial spin ice is spin Hall magnetoresistance (SMR) [77]. In ferromagnetic insulators such as yttrium iron garnet (YIG), it is not possible to directly pass a current and measure the magnetic transport properties. In insulating

materials, the SMR is exploited by using a conductor with a high spin Hall angle such as Pt in direct contact with the magnetic layer. When an electrical current flows in the heavy metal conductor, spin-orbit interaction separates electrons with opposite spins by means of the spin Hall effect [80, 81, 82], which effectively creates a spin current perpendicular to the charge current and spin accumulation arises at the surfaces. Spins with a normal component to the magnetization will transfer angular momentum to the magnetic material and, at the same time, a change in their spin direction will occur, resulting in a change in the resistance due to the inverse spin Hall effect [77].

3.2. Microwave spectroscopy

Microwave-based techniques are advantageous for studying dynamics in artificial spin ice due to their high sensitivity. Typically, a coplanar waveguide or stripline geometry in combination with a vector network analyzer ferromagnetic resonance technique (VNA-FMR) is used for these types of measurements [84]; see Fig. 5(a). For this purpose, the artificial spin ice can either be directly patterned on top of the signal line [85, 86, 87, 88] or the coplanar waveguide is fabricated on top of the ASI network. A schematic of the experimental setup is shown in Fig. 5(a). It was also shown that a so-called *flip-chip* method can be used [69, 72, 89]. In this case the artificial spin ice covers an extended area of the substrate material that is then placed on top of the antenna structure (e.g., coplanar waveguide). For the actual VNA-FMR measurements, a microwave signal is applied to the coplanar waveguide or microwave antenna. The accompanying microwave magnetic field (Oersted field) exerts a torque on the magnetization in the adjacent ferromagnet, which results in the onset of dynamics; see also Eq. 2. The transmitted or reflected microwave signal is then measured by the VNA; the absorbed power is a direct measure for the excited spin dynamics – at specific field and frequency values, the spins oscillate at a higher amplitude, resulting in a higher absorption. By varying the bias magnetic field it is possible to experimentally access the different modes in the magnetic nanostructures. Another possibility to measure ferromagnetic resonance is by using a microwave generator and antenna structure connected to a microwave diode detector [72]. Here, the microwave signal transmits microwaves through the antenna, effectively coupling microwave magnetic fields directly to the magnetic sample. The output of the antenna is then rectified using the microwave diode detector.

Another technique that is based on microwave excitation is spin-torque ferromagnetic resonance (ST-FMR), that was originally developed as a basic metrology to determine spin torques in magnetic/non-magnetic metal heterostructures [83, 90]. Here, a microwave charge current is directly passed through a heterostructure that consists of a ferromagnetic material capped with a heavy metal exhibiting significant spin-orbit coupling. Figure 5(b)-(d) illustrates the measurement configuration and basic principle of ST-FMR. The ferromagnet can either be metallic or insulating. In addition to the conventional Oersted field created by the *rf* charge current in the metal bilayer, an oscillating transverse spin current is generated in the heavy metal layer due to the spin Hall effect, see Fig. 5(b) and (c). This spin-polarized electron current is then injected into the ferromagnetic layer and the magnetization starts to precess when the condition for fer-

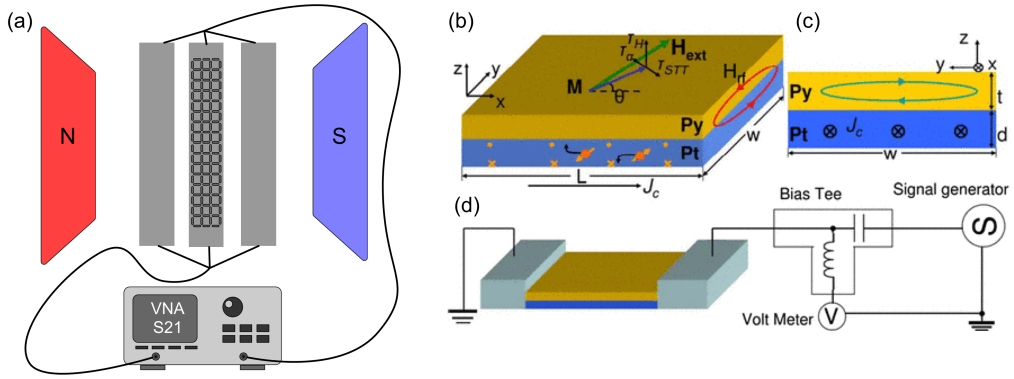

Figure 5. (a) Ferromagnetic resonance spectroscopy using a vector network analyzer. The artificial spin-ice structure is patterned on the signal line of a coplanar waveguide. The microwave transmission (S21) is recorded as a function of the external magnetic field. (b) Illustration of spin-torque ferromagnetic resonance technique: an alternating charge current is passed through a ferromagnet/heavy metal (Py/Pt) bilayer. The spin Hall effect in Pt causes spins pointing out of the plane to be deflected towards the Py layer. This spin current exerts a torque τ_{STT} on the magnetization M. In addition, the alternating charge current generates a Oersted field H_{rf}. (c) Side view of the Pt/Py bilayer system. (c) Measurement configuration for ST-FMR measurements: a bias-T allows for simultaneous microwave transmission and *dc* voltage detection via a voltmeter or lock-in amplifier. Adapted from [83].

romagnetic resonance is fulfilled. When the spin precession of the ferromagnetic layer is driven into resonant oscillations, this results in a concomitant oscillation of the bilayer resistance due to the anisotropic magnetoresistance (AMR) in case of a ferromagnetic metal, or spin Hall magnetoresistance (SMR) in case of a ferromagnetic insulator. The time-varying resistance $R(t)$ change leads to a *dc* spin rectification signal $V(t)$ across the length of the sample from the mixing of the resistance with the microwave current $I(t)$ via $V(t) = I(t) \cdot R(t)$. For micrometer sized films it was shown that depending on the relative phase of the driving torque with respect to the current the rectified *dc* voltage can be described by either a symmetric or antisymmetric Lorentzian function that depends on the applied magnetic field [83]. The detected *dc* spin rectification signal, V_{dc} has a shape of a mixed Lorentzian function:

$$V_{\mathrm{dc}} = -\frac{1}{4}\frac{dR}{d\theta}\frac{\gamma I_{\mathrm{rf}}\cos\theta}{\Delta(d\omega/dH)}C(H_{\mathrm{ext}})\,, \qquad (4)$$

where $C(H_{\mathrm{ext}}) = [SF_{\mathrm{S}}(H_{\mathrm{ext}}) + AF_{\mathrm{A}}(H_{\mathrm{ext}})]$. $F_{\mathrm{S}}(H_{\mathrm{ext}}) = \Delta^2/[\Delta^2 + (H_{\mathrm{ext}} - H_0)^2]$ is a symmetric Lorentzian function around H_0 and Δ is the linewidth. F_{A} is an antisymetric Lorentzian function given by $F_{\mathrm{A}}(H_{\mathrm{ext}}) = F_{\mathrm{S}}(H_{\mathrm{ext}})(H_{\mathrm{ext}} - H_0)/\Delta$, $S = \hbar J_{\mathrm{S}}^{\mathrm{rf}}/(2e\mu_0 M_{\mathrm{S}} t)$ with *rf* spin current density $J_{\mathrm{S}}^{\mathrm{rf}}$, thickness t, and $A = h_{\mathrm{rf}}(1 + \sqrt{4\pi M_{\mathrm{eff}}/H_{\mathrm{ext}}})$ with Oersted field h_{rf} and effective magnetization M_{eff}. R is the resistance of the sample, I_{rf} is the microwave current through the sample, and $\omega/2\pi$ is the resonance frequency. The antisymmetric Lorentzian is attributed to the effective field which includes Oersted field and field-like spin transfer torques. The anti-damping torque accounts for the symmetric Lorentzian signal. Using this approach and analyzing the magnitude of the two Lorentzian lineshapes it is even possible to determine the spin Hall angle of a material [83].

In this context, it is worth mentioning that it is possible to electrically drive spin dynamics in magnetic heterostructures. The spin Hall effect in a heavy metal layer can

be used to convert an electric charge current into a spin-polarized current. If this spin-polarized current is injected in an adjacent magnetic layer, the spin-polarized current exerts a torque on the magnetization. It can either favor or impede oscillations in the magnetic layer, depending on the direction of its spin-polarization vector. If the generated current compensates the internal damping, the magnetization starts to auto-oscillate without applying any *rf* current. The resonance frequency of the auto-oscillations depends on the applied magnetic field and the charge current density. Since the frequency of the auto-oscillation lies in the GHz range, it can be detected by a spectrum analyzer [91, 92, 93] or a diode detector [94]. It was shown that the onset of auto-oscillations can even be detected as a *dc* voltage variation [95]. Although auto-oscillations in ASI have not yet been experimentally demonstrated, it may be an interesting concept to use interconnected lattices for an electrical excitation of magnetization dynamics in these networks.

3.3. X-ray microscopy

For a variety of studies in magnetism, it is important to know the magnetic configuration of a material in the real space. For this purpose, X-ray microscopy techniques offer a unique opportunity due to their high resolution, element selectivity and even the possibility to perform time-resolved experiments in synchrotrons [96, 97, 98].

In photoemission electron micrsocopy (PEEM), X-ray radiation excites electrons in a material. Variations in the properties of the material (thickness, magnetization, composition, etc.) will result in a change in the intensity of the emitted electrons. The photoemitted electrons from the radiated samples are extracted by applying a large electric field and sent to an electron-to-visible-light detector, which finally produces an image detected by a CCD [99, 100]. When the incoming radiation is polarized, the absorption in a ferromagnetic material is dependent on the direction of the magnetization with respect to the polarization, an effect known as X-ray magnetic circular dicroism (XMCD) [101]. Owing to the XMCD effect, it is possible to produce an image of the magnetization. This technique has been successfully used in artificial spin ices to image emerging magnetic monopoles [102].

Time-resolved PEEM (TR-PEEM) measurements offer the unique opportunity to study magnetization dynamics with unprecedented spatial resolution. Time-resolved measurements are possible since the incident X-rays, produced in synchrotrons, are pulsed. This type of measurement can be used as a pump-probe technique that can be synchronised with a microwave excitation. TR-PEEM measurements have been used to image domain-wall motion [103, 104, 105], gyrotropic vortex motion [106, 107], and other dynamics in magnetic structures such as spin waves [108]. Time-resolved measurements using synchrotron pulsed X-rays can also be used to synchronise to other types of excitation such as surface acoustic waves [109]. For detailed reviews of X-ray PEEM and its use in magnetism, we refer to Refs. [110, 111, 112].

In scanning transmission X-ray microscopy (STXM), and full-field transmission X-ray micsroscopy (TXM), the X-rays are focused in the sample and the transmitted portion is detected with a photodiode [113]. The XMCD effect has also been used in this case to detect magnetization in the samples and observe the state in artificial spin ices [114].

Time-resolved measurements can also be done similar to TR-PEEM [115, 116, 117, 118]. For reviews of this technique we refer to [113, 119].

3.4. Brillouin light scattering spectroscopy

Brillouin light scattering (BLS) is an outstanding technique to measure spin waves and spin dynamics in magnetic materials. In a quantum mechanical picture, the BLS process can be described by the inelastic scattering of laser photons on magnons. The creation and annihilation of magnons upon scattering with a photon are both energy and momentum conserving processes [120]. Thus, the scattered photons carry information about the probed magnons: (1) Analysis of the frequency shift of the scattered photon yields information about the magnon frequency and (2) the momentum of the magnon can be probed by varying the incidence and detection angle of the laser light [120]. In addition, by studying the magnetic field dependence, the dispersion and magnonic band structure can be directly probed. In combination with microwave excitation certain magnon modes can be selectively populated and measured. For instance, the spin-wave propagation in magnetic waveguides can be studied in this way.

As outlined in Sec. 2, recent advances in micro- and nanofabrication enabled the fabrication of magnetic structures in the micrometer and even nanometer range. However, the laser focus of a conventional BLS system is tens of micrometers in diameter making it impossible to study individual magnetic micro- or nano-elements. In order to increase the spatial resolution the implementation of a scanning microscope with BLS is required. Typically, an objective with a magnification of 100x and a high numerical aperture (NA = 0.75) and a working distance of about 4 mm is used.

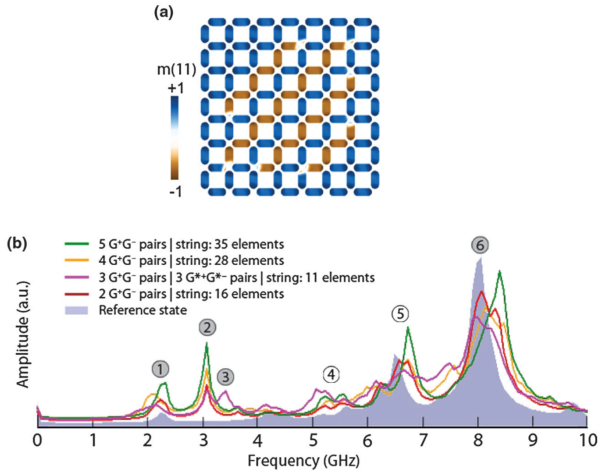

Figure 6. (a) Simulated network composed of 112 magnetic elements containing four monopole-antimonopole pairs connected by Dirac strings extending over 28 elements. (b) Simulated magnetization dynamics spectrum for increasing string length and number of monopole-antimonopole (G^+ and G^-) pairs compared to the reference state. Adapted from [25].

This results in a maximum spin-wave wavevector of $k_{\max} = 17.8\ \mathrm{rad}/\mu\mathrm{m}$ that can be detected with the BLS microscope corresponding to a spin-wave wavelength of 350 nm [120]. Further details about BLS spectroscopy especially devoted to imaging spin waves at the nanoscale can be found in a recent review article by Sebastian et al. [120].

4. Theoretical modeling and micromagnetics

Numerical simulations have been an important tool to study magnonic crystals and devices. The Landau-Lifshitz-Gilbert equation describes the time evolution of the magnetization, see Eq. 2. Including spin-torque effects leads to a modified version of the Landau-Lifshitz-Gilbert equation:

$$\frac{\mathrm{d}\mathbf{m}}{\mathrm{d}t} = -\gamma\mathbf{m}\times\mathbf{H}_{\mathrm{eff}} + \alpha\mathbf{m}\times\frac{\mathrm{d}\mathbf{m}}{\mathrm{d}t} + \frac{\gamma}{\mu_0 M_{\mathrm{S}}}\tau, \quad (5)$$

with $\mathbf{m}$ the normalized magnetization,γ the

gyromagnetic ratio, α the damping factor, $\mathbf{H}_{\text{eff}}$ the effective field, and

$$\tau = a(j)\,\mathbf{m} \times (\mathbf{m} \times \mathbf{j}) + b(j)\,\mathbf{m} \times \mathbf{j} \qquad (6)$$

is the Slonczewski spin-transfer-torque term produced by a charge current j. The effective field $\mathbf{H}_{\text{eff}}$ is composed of all magnetic fields acting on the system. Typically, for most micromagnetic simulations involving magnetization dynamics, the exchange, dipolar, anisotropy and Zeeman terms are used.

Finding the analytical solution of Eq. 5 is rarely possible, even in the case of a macrospin approximation. As such, a numerical solution is the usual approach. Typical tools for solving differential equations are used for this purpose. In micromagnetic simulations, the space is divided in a grid with cell sizes smaller than the exchange length, as the magnetization points in approximately the same direction below this length.

Since micromagnetic simulations have become an important tool in studying magnetization dynamics, there has been an increasing number of software packages available, such as OOMMF [121] and MuMax3 [122], as well as custom-built codes. The simulation of relatively large problems (above 1 μm lateral size) can be very computer-resource demanding. In order to increase the speed of the simulations, recent distributions of software such as MuMax3 make use of parallel GPU computing, exploiting graphic cards with thousands of computing cores originally developed for gaming and, more recently, big data analysis and bitcoin mining.

Gliga and co-workers were the first to study the eigenmode dynamics of topological defects in the magnetization, such as Dirac monopoles and Dirac strings, in artificial spin-ice structures using micromagmetic simulations [25]. These defects not only strongly affect the quasistatic and equilibrium behavior of the spin-ice network, but also exhibit distinct signatures in the mode spectrum. The resonances of a square spin-ice lattice consisting of 112 permalloy elements was modeled with micromagnetic simulations using a fully 3D finite-element algorithm based on the Landau-Lifshitz-Gilbert equation, see Fig. 6. Topological defects with charges ± 1 and ± 2 connected by strings of variable length were arbitrarily inserted in the lattice, see Fig. 6(a). The spin dynamics spectra were then obtained by applying a magnetic field pulse and integrating the Landau-Lifshitz-Gilbert equation in time. Figure 6(b) shows the simulated magnetization dynamics spectra for different number of monopole-antimonopole pairs and increasing string length. These results demonstrated that the presence of topological defects show a one-to-one correspondence with the spectral features and suggest that the presence of defects could in principle be experimentally identified in a microwave resonance experiment.

Micromagnetic simulations is an important tool to gain a deeper understanding of the spin dynamics in artificial spin ice and it has become a standard technique to design spin-ice lattices as well as to interpret the experimental results. Other theoretical methods include analytical formalisms [26] and computational methods based on the plane wave approach, e.g., [123].

5. Experimental results: Traditional spin dynamics and magnonics

While the majority of studies on artificial spin ice have focused on rather slow dynamics and thermalization processes, magnetization dynamics in the gigahertz regime in artificial spin ice have been explored only recently. Over the past five years, magnetization dynamics in the

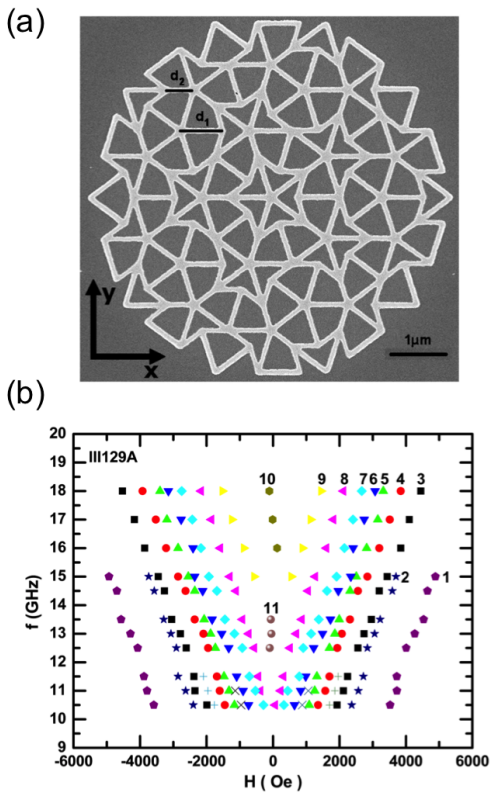

Figure 7. (a) Scanning electron microscopy image of a third-generation P2 tiling, where bright and dark regions correspond to permalloy and the Si substrate, respectively. (b) FMR frequency f vs dc magnetic field H plot. Numbers denote mode branches, where 10 and 11 correspond to asymmetric modes that only appear on one side of the field origin in a given sweep. Adapted from [124].

GHz regime has been experimentally studied in different types of ASI. In the following, we review different lattices and geometries and discuss the influence of the specific patterns on the magnetization dynamics. First, we discuss artificial quasicrystals in Sec. 5.1 as these systems were among the first nanopatterned arrays of ferromagnets studied in the high-frequency regime. We then discuss various aspects of artificial square lattices (Sec. 5.2). In particular, we first review experiments utilizing ferromagnetic resonance measurements and then continue with works using Brillouin light scattering spectroscopy. In Sec. 5.3 experimental results on the Kagome lattice are reviewed and Sec. 5.4 is devoted to a new type of ASI, which utilizes the gyrotropic motion of magnetic vortices.

5.1. Artificial quasicrystals

Among the first experimental studies on magnetization dynamics in artificial spin ice [69, 72, 85, 89, 124], were investigations on permalloy films patterned into artificial quasicrystals. These artificial quasicrystals consist of tilings that show long range order, but lack translational symmetry. They are locally self-similar and can continuously fill all available space. Bhat et al. [124] presented a detailed study on dc magnetization and ferromagnetic resonance absorption on quasicrystalline Penrose P2 tilings. A scanning electron microscopy (SEM) image of a third generation P2 tiling fabricated using electron beam lithography is displayed in Fig. 7(a). Reproducible knees in the dc magnetization were observed in the low-field regime. Their number and size depend on the temperature and the P2 tiling generation as confirmed by micromagnetic simulations using the OOMMF code. Interestingly, the switching events of individual segments is accompanied by a local FMR response of clusters of segments with several magnetic field directions. The orientation of those clusters with respect to dc field also strongly affects the static and dynamic magnetization in the near-saturated regime for fields larger than 1 kOe. Furthermore, the FMR spectra of the 8th generation P2 tiling exhibit tenfold rotational symmetry in the near-saturated regime, which is only expected for infinite P2 tilings. Figure 7(b) shows the FMR frequency vs applied field data. "Asymmetric" modes appear on only one side of the field origin in a given sweep,

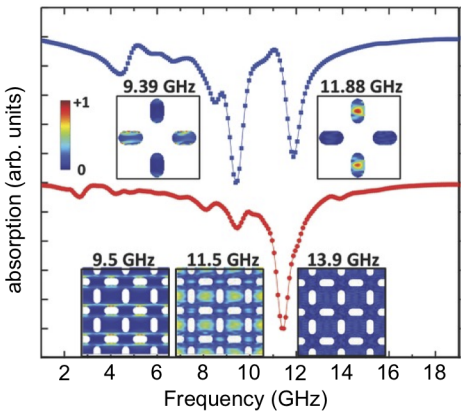

Figure 8. Micromagnetic simulations of the dynamic behavior of square artificial spin ice lattices. The simulations show oscillation amplitude in a color scale, which allows the identification of oscillation modes in the lattice. Comparison between the simulated frequency response of the absorption and the spatial oscillation amplitude at specific frequencies for a square ASI (top) and an square anti-ASI (bottom). Adapted from [69].

which correlates with the knees observed in the *dc* magnetization measurements in the low-field regime. The results demonstrate that pinning of the magnetization and confinement of domain walls at the vertices control segment polarization and low-field reversal. In principle, the observed pinning should also influence the spin-wave propagation in P2 tilings offering new perspectives for magnonic crystals.

5.2. Artificial square and anti-square lattices

Square ASI networks are the most common structures for the investigation of high-frequency characteristics. In this section, we present important results using two complementary measurement techniques, which were used to study artificial square lattices – ferromagnetic resonance [Sec. 5.2.1] and Brillouin light scattering [Sec. 5.2.2]. The corresponding techniques are reviewed in Sec. 3.

5.2.1. Ferromagnetic resonance The first experimental investigations on a square ASI with two different sublattices were presented by Sklenar et al. [72], where broadband ferromagnetic resonance measurements with a microwave meanderline technique were used. Along the primary axis of the ASI network, only one mode was observed at all frequencies. However, for a narrow angular range between 60° and 75° a history-dependent high-field signal was observed asymmetrically about zero field. The data suggest that this behavior is due to the local configuration of nearby islands that could be changing state when the field is swept. More detailed studies on the hysteretic behavior of a square ASI were reported in Ref. [85], which we discuss in more detail below.

Large arrays of square spin ices and anti-square spin ices (ASSI) were studied by Zhou et al. [69]. First studies on ASSI were presented by de Araujo et al. [74], in which they studied the possibility to form magnetic vortices in the center regions to create a connected lattice of magnetic vortices. Ribeiro et al. showed angular-dependent ferromagnetic resonance measurements on the same kind of ASSI containing magnetic vortices [75]. Zhou et al. could fabricate large-area ASI and ASSI structures by DUV lithography allowing for measurements of static magnetization loops by magnetic force microscopy and vibrating sample magnetometry, which were correlated with the FMR results. Angular-dependent dynamic measurements revealed two resonant peaks that decreased in frequency as the field was reduced. Their angular dependence at a constant magnetic field showed a reciprocal fourfold symmetry, that is, the frequency of one of the peaks was maximum at 0° and minimum at 90° whereas the frequency of

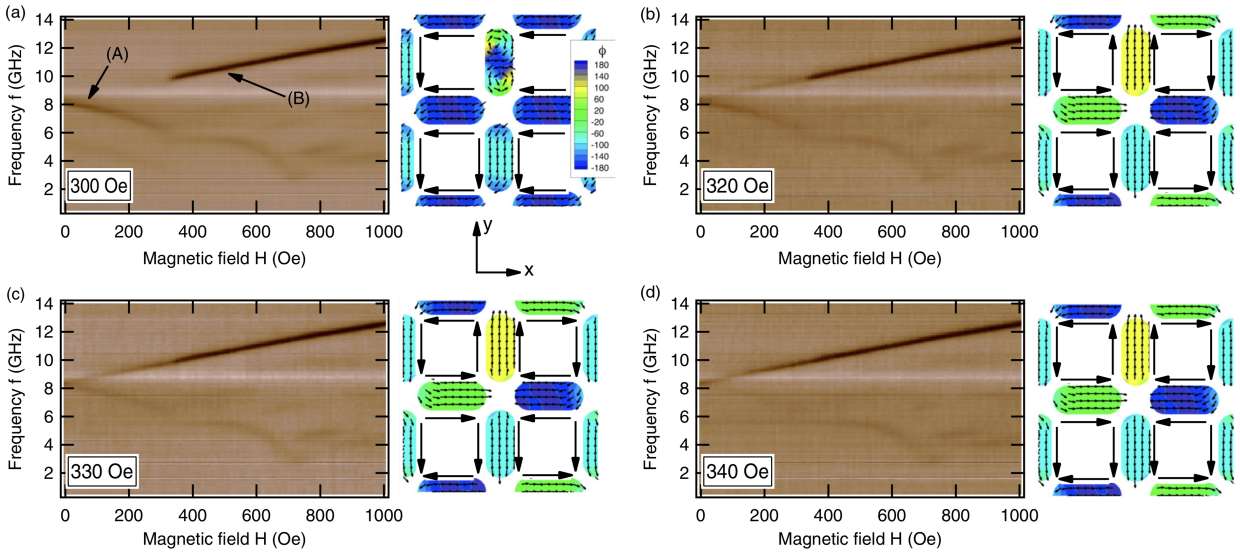

Figure 9. Hysteretic behavior observed in square spin ice at low applied magnetic fields. The following minor loop routine was applied: saturating the system at −3100 Oe, then set the initialization field $H_{\rm ini}$ record the spectrum starting at 0 Oe while gradually increasing the applied field. (a) - (d) $H_{\rm ini}$ was varied from 300 Oe to 340 Oe. At 300 Oe, the modes (A) and (B) do not coexist at zero field, (a), but as the field increases mode (B) appears at lower fields, (b) and (c). Increasing $H_{\rm ini}$ beyond 330 Oe results in a disappearance of (A) at H = 0 Oe, (d). The simulated magnetization states at zero field are shown next to each spectrum with the color coding indicating the azimuthal in-plane angle of the magnetization. Adapted from [85].

the other peak was minimum at 90° and maximum at 0°. At an angle of 45°, both frequencies overlapped. These results indicate that the dynamic response was dominated by the magnetostatic interactions in the equally oriented islands, where each sublattice has a different characteristic frequency due to the shape anisotropy. Micromagnetic simulations confirmed the contributions of the differently oriented sublattices. The magnetization of the structures was simulated as a function of time after a field pulse was applied. Fast Fourier Transforms (FFT) on the 2D spatial profile of the structure were then used to understand in which region the magnetization dynamics was excited at each frequency, see Fig. 8.

In minor loop experiments the maximum external field values are chosen low enough so that the magnetization in the studied nanostructures is not (completely) switched. A correlation between eigenmode dynamics and the magnetization state of the ASI network then allows to identify the different modes in a resonance experiment. A detailed study of this correlation between the switching of individual elements in a square ASI and ferromagnetic resonance measurements was presented in Ref. [85], see Fig. 9. A hysteresis in the low field regime was observed in the dynamic response. For this purpose the sample was first saturated at a high bias magnetic field in the $-x$ direction and then the magnetic field was reversed to a smaller field $H_{\rm ini}$ as indicated in the Fig. 9. Afterwards, the magnetic field was set to $H = 0$ Oe and the spectra were recorded while the field was gradually increased, see Fig. 9(a) - (d). In Fig. 9(a) the two main modes labeled as (A) and (B) do not coexist at zero field. As the field $H_{\rm ini}$ was increased, mode (B) starts to appear at smaller applied fields H, see

Figs. 9(b) and (c). In Fig. 9(c) both modes (A) and (B) do coexist at H = 0 Oe. Increasing H_{ini} even further leads to a disappearance of mode (A) at $H = 0$ Oe and only mode (B) persists [Fig. 9(d)]. This result clearly showed the existence of field-dependent hysteresis in the spin-ice system, which was also reported in Ref. [72]. By comparing the experimentally acquired FMR spectra with the equilibrium magnetization at zero field obtained from micromagnetic simulations following the same protocol as in the experiment, it became clear that the field range where the change in the static magnetization at zero field occurs agrees well with the experimentally observed onset of hysteresis in the dynamic response, see Fig. 9.

5.2.2. Brillouin light scattering Li et al. [125] studied the thermal magnetic excitation spectrum in a square ASI by wavevector-resolved Brillouin light scattering. As discussed in detail in Sec. 3.4, the incidence and detection angle of the probing BLS laser was varied to measure the in-plane spin-wave wavevector component. Li and co-workers studied spin dynamics by BLS in two different configurations: (1) in the Damon-Eshbach configuration, where the spin-wave vector is perpendicular to the external magnetic field, and (2) in the backward-volume configuration, where the spin-wave wavevector is parallel to the external magnetic field. Furthermore, they varied the orientation of the ASI lattice with respect to the external magnetic field. An overview of the different configurations is shown in the top panel of Fig. 10. The bottom panel in Fig. 10(a)-(d) presents the corresponding wavevector-resolved BLS measurements. As is apparent from the spectra, several high-frequency modes could be detected. BLS can in principle detect excitations that may not be visible in FMR measurements since FMR is mainly sensitive to long wavelength modes. However, Li et al. found dispersion curves for Damon-Eshbach and backward-volume modes that are almost flat. This indicates that any magnonic dynamic inter-island coupling can be ruled out in the studied lattice. In order to interpret the experimental data, Li et al. performed micromagentic simulations using MuMax3. Based on those simulations they could identify the spatial profiles of single elements and distinguish between backward volume, Damon-Eshbach, edge-like, and fundamental modes. The simulated spatial amplitude of the oscillations of these modes is shown in Fig. 10(e). EM denotes edge modes, while DE denotes Damon-Eshbach modes and F is the fundamental mode. They concluded that inter-element interactions were negligible and the dynamics could be modelled mainly as an ensemble of independent elements pointing in different directions with respect to the magnetic field.

Another type of ASI is anti-square lattices consisting of extended films with elongated holes as individual elements [74, 75]. Anti-ASI lattices were also studied by FMR [69, 75] and BLS [123]. FMR results indicated that the dynamic response mainly comes from the predominant collective mode produced by the extended magnetic areas between the holes, shown in the bottom red curve and insets of Fig. 8, as well as from some minor modes that increased their intensity as the angle between the external field and the square lattice was changed to 45°. This observation was attributed to an increase in the magnetostatic interactions and edge modes. Additional BLS measurements in combination with a theory based on the plane-wave method by Mamica et al. [123] gave a deeper understanding of the spin dynamics in the anti-spin-ice system, see Fig. 11. Figure 11(a) shows the experimen-

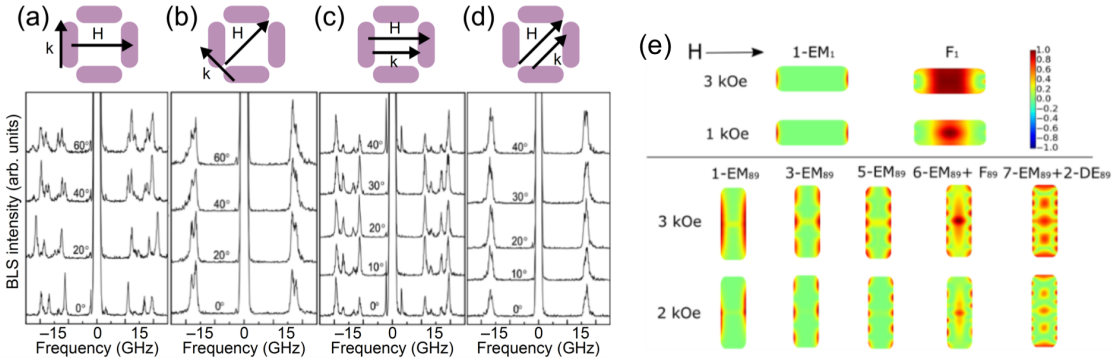

Figure 10. BLS spectra of a square ASI with different field-wavevectors orientations, at incident angles 0°, 20°, 40° and 60°. (a) Damon-Eshbach modes with the field applied parallel to the square lattice direction. (b) Damon-Eshbach modes with the field applied along the diagonal of the square lattice. (c) Backward modes with the field applied along the square lattice. (d) Backward modes with the field applied along the diagonal of the square lattice. (e) Simulated spatial oscillation amplitude of a single element of a square ASI at different field orientations, showing a variety of oscillation modes. Adapted from [125].

tally obtained wavevector-resolved BLS measurements (blue symbols) and a comparison to the calculations (brown lines). A transformation of the spectra from predominantly non-propagative spin waves into the spectra of propagating spin waves with a number of hybridizations could also be obtained by rotating the external magnetic field by 45°. The results of the corresponding calculated 2D maps of the spin-wave profiles are shown in Fig. 11(e)-(g). Each mode is a representative of one of the BLS bands shown in Fig. 11(a). For instance, the mode profile shown in Fig. 11(b) is the lowest mode visible in the BLS spectrum for $k = 0$. As is evident from the mode profile, the spin-wave amplitude is confined to small areas along sides of holes perpendicular to the field direction. The profiles for the higher-frequency bands observed by BLS are shown in Fig. 11(b)-(g). All these modes are confined almost in the same region between the holes. As a consequence, spin waves tend to have a small group velocity and flat bands are observed in the BLS spectra, Fig. 11(a).

The BLS measurements reported to date confirm the corresponding results obtained by FMR. Despite these recent efforts, a clear one-to-one correspondence of localized magnetization dynamics in the ASI structure and defect strings as well as their interplay is missing. Spatially-resolved BLS could potentially be employed to address this question as indicated by recent experiments by Bhat and Grundler [126].

5.3. Artificial Kagome lattice

Among different types of ASI, artificial Kagome lattices are particularly interesting since they are intrinsically frustrated systems. They consist of an hexagonal lattice and, hence, there are three intersecting bars at each vertex. The ice rules in this case indicate that the state of minimum energy is a configuration of two-in/one-out or two-out/one-in, as shown in Fig. 2(b).

Bhat et al. [89] reported microwave spectroscopy on a large array of a Kagome lattice. The experimental results showed four different modes with different behaviors as a function of the applied field. Only one of the modes was visible over the

entire field sweep, which was linked to the precession of the magnetization aligned with the magnetic field. As the islands were reversed, the slope of this mode changed, and one of the modes, associated with the precession of the magnetization that pointed opposite to the magnetic field, re-appeared. Micromagnetic simulations using OOMMF revealed the different contributions of the differently oriented parts of the ice. The appearance of Dirac strings – i.e. strings in the magnetization without any discontinuity – in Kagome lattices where also identified in the simulations, as they gave rise to characteristic resonances that are observable in experiments.

The angular dependence of the resonant lines [127], alongside with the micromagnetic simulations, also pointed towards the characteristic dynamics of the differently oriented parts of the lattice. It was found that as the magnetic field was swept particular modes appeared in the resonance spectra associated with the switching of different parts of the lattice. The field values of the switching events depend on the angle at which the magnetic field is applied with respect to the direction of the magnetization in the island. Moreover, Bhat et al. presented a comparison of the dynamics obtained from micromagnetic simulations of interconnected lattices and disconnected lattices. The different dynamics indicate the importance of the vertex regions in this geometry.

This also plays an important role in the dynamics of the reversal process of the magnetization. Near the reversal field, the magnetization of individual elements starts to curl around the edges, making a macrospin approximation less accurate. Montoncello et al. [86] studied the reversal dynamics of a single Kagome vertex comparing micromagnetic simulations and experimental

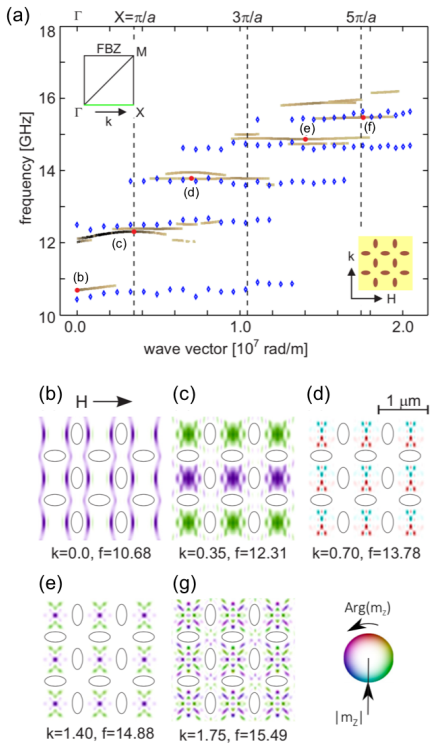

Figure 11. (a) Comparison of wavevector-resolved BLS data (blue data points) and theoretical results obatined by the plane wave method (brown lines). (b)–(g) Simulations of a square anti-ASI showing different modes characterized by their oscillation amplitude and phase. Adapted from [123].

FMR data. The study focused on the dynamics of two types of vertices: (i) three equally shaped ellipses at 120° angle between each other, and (ii) two equally shaped ellipses and a narrower ellipse at 120° angle. Using micromagnetic simulations, Montoncello et al. identified field-dependant modes localized at the different elements in the vertex region. Since the field distribution is not uniform, the fundamental mode splits in different regions of the system with different effective field values. In the case of equally shaped ellipses, the non-uniform field distribution results in two different fundamental modes; one localized in the element parallel to the magnetic field that is highly hybridized, and the other localized in the other two elements

that are equally oriented with respect to the magnetic field. As the field approaches the critical value for the reversal, a soft mode arises, merges with the fundamental mode and becomes the predominant mode. The soft mode is characterized by a quickly decreasing resonance frequency as the field is reduced. A higher-frequency backward-volume mode was detected for the equally-shaped ellipses. It is important to note that not all simulated modes can always be measured in experiments, since the signal in FMR is proportional to the volume of the magnetic material, which might result in a signal that is too weak to be detected experimentally. This was verified by reducing the thickness of the symmetric sample leading to the disappearance of the volume mode [86].

5.4. Other types of lattices: Vortex ASI

As outlined in the previous sections, ASI structures are typically composed of either separated interacting magnetic islands, or by interconnected elements that ultimately allow transport measurements, see Sec. 3.1. However, it is also possible to construct an ASI consisting of interacting sub-elements. For instance, interacting coupled disks were used as the base element of a Kagome artificial spin ice [117]. A scanning electron microscopy image of the studied lattice is shown in Fig. 12(a). By tuning the shape of the disks, it is possible to realize a ground state consisting of a magnetic vortex [129, 130, 131, 132]. In general, a magnetic vortex in a disk is characterized by an in-plane curling magnetization and an out-of-plane core [133, 134, 135, 136]. The direction of the core determines the sense of the gyrotropic motion, i.e. the resonant oscillation of the core around its equilibrium position [106, 137, 138, 139]. It was shown that high-amplitude rf excitations at the gyrotropic frequency can be used to reverse the core orientation [140, 141, 142]. Since the magnetization texture in disks is far from a macrospin approximation, the Ising model is no longer applicable. As a result, the characteristic behavior of magnetic vortices can be used to modify the artificial spin ice instead. By applying high amplitude field excitations H_{state} at different frequencies, Behncke et al. indeed showed in FMR and STXM measurements that the ground state of the lattice can be modified [117]. Depending on the excitation frequency, the ground state could be selected to behave as a frustrated spin ice or as a long-range

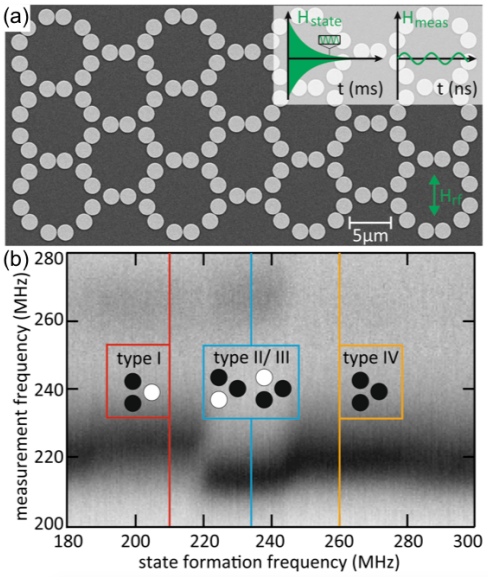

Figure 12. (a) Scanning electron micrograph of magnonic vortex crystals. A copper stripline is placed on the Py disks to excite the gyrational motion of the vortices. The polarization pattern is tuned via an adiabatic reduction of a microwave magnetic field excitation H_{state}. A low-amplitude harmonic field H_{meas} excites the vortices during the FMR and STXM measurements. (b) Ferromagnetic absorption spectra for different state formation frequencies. The insets show the most common triple types and their corresponding state formation frequency (solid lines). Adapted from [117].

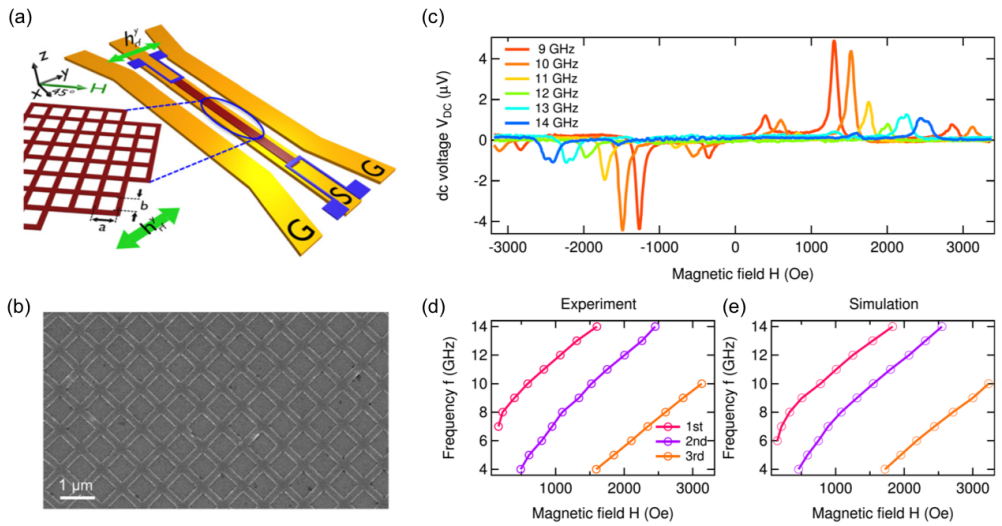

Figure 13. (a) Schematic of the experimental setup. The ASI lattice is oriented at 45° with respect to the signal line S. (b) Example of a scanning electron microscopy image; $a = 845$ nm and $b = 585$ nm. (c) Typical *dc* voltage spectrum for different applied microwave frequencies. The resonance signals show a mostly symmetric Lorentzian lineshape and change their polarity upon field reversal. (d) Comparison of different modes in a frequency vs. field plot as extracted from the spectrum shown in (c). (d) Corresponding simulated frequency vs. field relation obtained using MuMax3. Adapted from [128].

interacting system without frustration. The corresponding FMR absorption measurements are shown in Fig. 12(b).

6. Experimental results: Spin-transport related phenomena

The utilization of electron-carried spin and charge currents opened entirely new perspectives in magnonics. Magnon spintronics is concerned with the transport and processing of information in magnon-based circuits and to interconvert magnon currents and electronic spin currents [17]. The promise here is to harness the unique and controllable magnon characteristics for novel device architecture where information encoded in a magnonic signal and an electronic signal can be interconverted. This has been shown for a wide variety of material classes including magnetic insulators and metals, e.g., [83, 92, 143, 144, 145, 146, 147, 148]. Usually, macroscopic samples or patterned structures with lateral dimensions of tens to hundreds of micrometers are used in these kinds of spin pumping and spin-torque experiments.

6.1. Electrical detection and excitation of dynamics in ASI

Recently, it was shown that the standard spin-transport metrologies as outlined above can be used to detect spin dynamics in ASI [128], Fig. 13. In these measurements, the ASI network is made of a bilayer consisting of a ferromagnetic metal layer (Py) and a heavy metal layer (Pt). The connected square ASI network [Fig. 13(b)] is deposited on top of a coplanar waveguide and additional leads are added so that an electric current can be measured or applied, see Fig. 13(a). It was demonstrated that Oersted-driven dynamics in the Py layer can pump a spin-polarized electron current in the adjacent Pt layer,

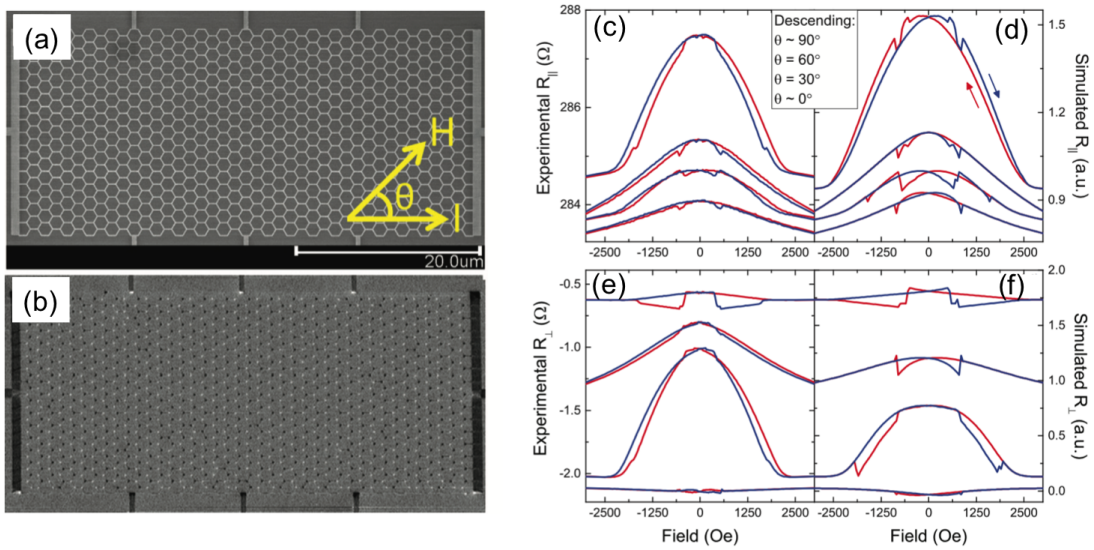

Figure 14. Magnetic transport measurements on Kagome artificial spin ice network. (a) Scanning electron microscopy image. An external magnetic field H is applied in-plane; θ is the angle between the field direction and the nominal current direction, I. (b) Corresponding magnetic force microscope. (c) Experimental longitudinal magnetoresistance, (d) experimental transverse magnetoresistance. (e) and (f) Corresponding simulated longitudinal and transverse magnetoresistance data. The down field sweeps (red) and up field sweeps (blue) are symmetric under field inversion. Adapted from Ref. [54].

where the spin current is converted into an electric charge current by means of the inverse spin Hall effect. Hence, peaks in the electric signal were observed when the condition for resonance was achieved, see Fig. 13(c). Micromagnetic simulations using MuMax3 confirmed the experimental results, where three distinct modes were detected, see Fig. 13(c)-(d).

Furthermore, spin-torque ferromagnetic resonance investigations in a square ASI system were demonstrated and correlated to magneto-transport measurements [79]. From this end, it is important to understand the magnetic transport data in ASI, which is discussed in the next section.

6.2. Correlation between magnetic transport data and dynamics

As detailed in Sec. 3.1, transport measurements can be a useful tool to understand the equilibrium states of ASI [32, 52, 53, 54, 55, 79] and may even provide insights in the spin dynamics excited in the structures.

Various aspects of magnetoresistance in ASI have been studied in the past decade [32, 52, 53, 54, 55]. For instance, Branford et al. studied the emergent chirality in a honeycomb ASI at low temperatures by analyzing the different resistance contributions, i.e. parallel or perpendicular to the current with varying field orientations [53]. Le et al. [54] measured AMR of a Kagome lattice and by comparison with micromagnetic simulations they showed that the vertex region dominates the AMR response of the entire lattice. Figure 14(a) shows a scanning electron microscopy image of the device, while Fig. 14(b) shows the corresponding magnetic force microscopy image with black and white dots at the vertices indicating magnetic domain walls. The AMR response was modelled by calculating the path

integral $\Delta V = \int \mathbf{E} \cdot \mathrm{d}\mathbf{l}$ using the simulated electric field $\mathbf{E}$ produced by the magnetic ice [see Eq. (1)] and assuming a non-uniform current distribution, as shown in Fig. 15 [149]. A remarkable agreement between this simple model and the experimentally acquired field traces was found, as can be seen by comparing the experimental data in Fig. 14(c), (d) and simulation results (e), (f).

Recently, a combination of magnetic transport measurements and ST-FMR measurements was used to correlate the anomalies in the two types of measurements [79]. During the collective reversal of the magnetic islands in the network, sharp features in the MR were found, which were reproduced by micromagnetic simulations. The experimental dynamic data showed an unusual resonant absorption during the reversal, indicating that the vertex magnetization processes also define the dynamics of the spin ice. This agrees well with the FMR measurements on connected lattices such as artificial quasicrystals discussed in Sec. 5.1. These observations are first steps towards the integration of ASI networks in more complex magnon spintronic device architectures and eventually may lead to reconfigurable microwave oscillators and magnetoresistive devices based on connected networks of nanomagnets.

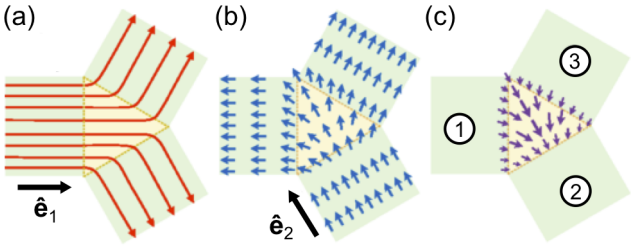

Figure 15. Schematics showing the computation of the electric field created by AMR of a vertex of a connected honeycomb lattice. (a) Current distribution. (b) Magnetization profile considering an one-in-two-out ice rule. (c) Resulting electric field proportional to the product of the distributions in (a) and (b), as expressed in Eq. 1 described in the text. Adapted from [149].

7. Summary and outlook

The exploration of spin dynamics in nanopatterned arrays of ferromagnets is an interesting research area from a fundamental physics point of view, but also for the development of potential applications based on magnonic devices.

Over the past two decades, there has been a significant progress on the understanding of dynamics in magnetic nanostructures. The investigation of arrays of simple ferromagnetic elements have lead to our current understanding of magnetization dynamics at the micrometer- and nanometer scale. Enabled by modern lithography creative lattices can be realized that were impossible to fabricate before. Artificial spin ice is one example of these kinds of structures. Originally, these lattices made of ferromagnetic elements were envisioned to be a model system to study frustration. However, looking at the magnonic and spintronic properties of artificial spin ice opens a new playground to explore the interplay between frustration and control of spin-wave properties.

The works presented in this Topical Review suggest that spatially localized modes are responsible for the formation of spin-wave band gaps. Having the ability to reconfigure the artificial spin ice on demand, for instance by spin-torque effects, may lead to new types of magnonic crystals and microwave oscillators. Studies of the interaction between resonant magnetization dynamics and defect strings connecting monopole-antimonopole pairs in the networks have just begun [25, 89, 127]. The implementation of spin-torque effects to locally switch the magnetization would be an interesting pathway for a targeted control of

defect strings in the 2D lattices. In this regard, it is interesting to note that Luo et al. recently designed magnetic domains in Pt/Co/AlOx with alternating in-plane and out-of-plane magnetization due to interfacial Dzyaloshinskii-Moriya interaction [150]. They were able not only to engineer various magnetization textures such as skyrmions and ASI, but also to achieve a field-free current-induced switching in the elements. This result opens doors to completely new opportunities in ASI in general, and magnonics with ASI in particular. Using layered structures or dissimilar materials in the same lattice may be an alternative way to realize the same goal.

Exploring a broader range of materials such as the ferrimagnetic insulator yttrium iron garnet for the fabrication of ASI is particularly interesting for magnonic applications due to the low Gilbert damping of yttrium iron garnet [151]. Another approach could be to use spin Hall magnetoresistance effects in yttrium iron garnet/platinum heterostructures instead of anisotropic magnetoresistance in ferromagnetic metals. In terms of new material categories, it is interesting to note the recent work by Wang et al. [40]. They reported a magnetic artificial spin ice that was patterned on top of a superconductor. Using this type of heterostructure new phenomena were revealed, which are not achievable in either of the subsystems.

In this Topical Review we have mainly discussed artificial spin-ice networks with elongated nanomagnets that behave like Ising spins; i.e., the magnetization in the islands have two orientations and thus exhibit binary degrees of freedom. However, recent experimental efforts demonstrate that one can design and develop spin lattices that go beyond the Ising model [38]. By tuning either the topology or the shape/crystalline anisotropy it is possible to create new spin-lattice models with more than two degrees of freedom resembling an artificial Potts spin system [152] or even more exotic spin-lattice models such as XY and Heisenberg spin systems. These systems have been shown to exhibit new magnetic orders and rich phase diagrams. From a dynamic perspective, it is interesting to explore how the predominant interactions modify the high frequency response of those systems.

Despite the progress in detecting spin dynamics in artificial spin ice by optical techniques such as Brillouin light scattering spectroscopy, a clear one-to-one correspondence of defect strings and magnetization dynamics in 2D is missing. Spatially-resolved Brillouin light scattering measurements could potentially close this gap [126].

Another interesting direction is the utilization of artificial spin ice for logic and computational applications; e.g., [153, 154, 155]. The implementation of artificial spin ice was also discussed for novel types of neuromorphic computing concepts [156]. From this end, the integration of spin-torque oscillators and magnetoresistance devices in artificial spin ice might provide desirable functionalities [156] and lead to concepts that are important for next-generation computing and memory devices.

8. Acknowledgment

The authors thank Dr. Joseph Sklenar for valuable discussions and proofreading of this manuscript. This work was partially supported by the National Science Foundation under Grant No. 1833000.

9. References

[1] Harris M J, Bramwell S T, McMorrow D F, Zeiske T and Godfrey K W 1997 *Phys. Rev. Lett.* **79** 2554–2557

[2] Bramwell S T and Gingras M J P 2001 *Science* **294** 1495–1501

[3] Castelnovo C, Moessner R and Sondhi S L 2008 *Nature* **451** 42

[4] Bramwell S T, Giblin S R, Calder S, Aldus R, Prabhakaran D and Fennell T 2009 *Nature* **461** 956

[5] Morris D J P, Tennant D A, Grigera S A, Klemke B, Castelnovo C, Moessner R, Czternasty C, Meissner M, Rule K C, Hoffmann J U, Kiefer K, Gerischer S, Slobinsky D and Perry R S 2009 *Science* **326** 411–414

[6] Fennell T, Deen P P, Wildes A R, Schmalzl K, Prabhakaran D, Boothroyd A T, Aldus R J, McMorrow D F and Bramwell S T 2009 *Science* **326** 415–417

[7] Wang R F, Nisoli C, Freitas R S, Li J, McConville W, Cooley B J, Lund M S, Samarth N, Leighton C, Crespi V H and Schiffer P 2006 *Nature* **439** 303–306

[8] Nisoli C, Moessner R and Schiffer P 2013 *Rev. Mod. Phys.* **85** 1473–1490

[9] Gilbert I, Nisoli C and Schiffer P 2016 *Phys. Today* **69** 54–59

[10] Heyderman L J and Stamps R L 2013 *J. Phys.: Condens. Matter* **25** 363201

[11] Mól L A, Silva R L, Silva R C, Pereira A R, Moura-Melo W A and Costa B V 2009 *Journal of Applied Physics* **106** 063913

[12] Morgan J P, Stein A, Langridge S and Marrows C H 2011 *Nat. Phys.* **7** 75–79

[13] Zabel H and Farle M 2012 Magnetic nanostructures: spin dynamics and spin transport

[14] Chumak A V, Serga A A and Hillebrands B 2017 *J. Phys. D: Appl. Phys.* **50** 244001

[15] Neusser S and Grundler D 2009 *Adv. Mater.* **21** 2927–2932

[16] Lenk B, Ulrichs H, Garbs F and Münzenberg M 2011 *Phys. Rep.* **507** 107–136

[17] Chumak A V, Vasyuchka V I, Serga A A and Hillebrands B 2015 *Nat. Phys.* **11** 453–461

[18] Wang Z K, Zhang V L, Lim H S, Ng S C, Kuok M H, Jain S and Adeyeye A O 2009 *Appl. Phys. Lett.* **94** 083112–4

[19] Chumak A V, Serga A A, Hillebrands B and Kostylev M P 2008 *Appl. Phys. Lett.* **93** 022508

[20] Qin H, Both G J, Hämäläinen S J, Yao L and van Dijken S 2018 *Nat. Commun.* **9** 5445

[21] Goto T, Shimada K, Nakamura Y, Uchida H and Inoue M 2019 *Phys. Rev. Appl* **11** 014033

[22] Langer M, Gallardo R A, Schneider T, Stienen S, Roldán-Molina A, Yuan Y, Lenz K, Lindner J, Landeros P and Fassbender J 2019 *Phys. Rev. B* **99** 024426

[23] Chumak A V, Pirro P, Serga A A, Kostylev M P, Stamps R L, Schultheiss H, Vogt K, Hermsdoerfer S J, Laegel B, Beck P A and Hillebrands B 2009 *Appl. Phys. Lett.* **95** 262508

[24] Vogel M, Chumak A V, Waller E H, Langner T, Vasyuchka V I, Hillebrands B and von Freymann G 2015 *Nat. Phys.* **11** 487

[25] Gliga S, Kákay A, Hertel R and Heinonen O G 2013 *Phys. Rev. Lett.* **110** 117205

[26] Iacocca E, Gliga S, Stamps R L and Heinonen O 2016 *Phys. Rev. B* **93** 134420

[27] Gardner J S, Dunsiger S R, Gaulin B D, Gingras M J P, Greedan J E, Kiefl R F, Lumsden M D, MacFarlane W A, Raju N P, Sonier J E, Swainson I and Tun Z 1999 *Phys. Rev. Lett.* **82** 1012–1015

[28] Bramwell S T and Gingras M J 2001 *Science* **294** 1495–501

[29] Remhof A, Schumann A, Westphalen A, Zabel H, Mikuszeit N, Vedmedenko E Y, Last T and Kunze U 2008 *Phys. Rev. B* **77** 134409

[30] Qi Y, Brintlinger T and Cumings J 2008 *Phys. Rev. B* **77** 094418

[31] Nisoli C, Li J, Ke X, Garand D, Schiffer P and Crespi V H 2010 *Phys. Rev. Lett.* **105** 047205

[32] Tanaka M, Saitoh E, Miyajima H, Yamaoka T and Iye Y 2006 *Phys. Rev. B* **73** 052411

[33] Li J, Ke X, Zhang S, Garand D, Nisoli C, Lammert P, Crespi V H and Schiffer P 2010 *Phys. Rev. B* **81** 092406

[34] Drisko J, Marsh T and Cumings J 2017 *Nat. Commun.* **8** 14009

[35] Morrison M J, Nelson T R and Nisoli C 2013 *New J. Phys.* **15** 045009

[36] Zhang S, Gilbert I, Nisoli C, Chern G W, Erickson M J, O'Brien L, Leighton C, Lammert P E, Crespi V H and Schiffer P 2013 *Nature* **500** 553–557

[37] Sklenar J, Lao Y, Albrecht A, Watts J D, Nisoli C, Chern G W and Schiffer P 2019 *Nat. Phys.* **15** 191–195

[38] Louis D, Lacour D, Hehn M, Lomakin V, Hauet T and Montaigne F 2018 *Nat. Mater.* **17** 1076

[39] Canals B, Chioar I A, Nguyen V D, Hehn M, Lacour D, Montaigne F, Locatelli A, Menteş T O, Burgos B S and Rougemaille N 2016 *Nat. Commun.* **7** 11446

[40] Wang Y L, Ma X, Xu J, Xiao Z L, Snezhko A, Divan R, Ocola L E, Pearson J E, Janko B and Kwok W K 2018 *Nat. Nanotechnol.* **13** 560–565

[41] Wang Y L, Xiao Z L, Snezhko A, Xu J, Ocola L E, Divan R, Pearson J E, Crabtree G W and Kwok W K 2016 *Science* **352** 962–966

[42] Gliga S, Hrkac G, Donnelly C, Büchi J, Kleibert A, Cui J, Farhan A, Kirk E, Chopdekar R V, Masaki Y, Bingham N S, Scholl A, Stamps R L and Heyderman L J 2017 *Nature Materials* **16** 1106–1111

[43] Nisoli C, Wang R, Li J, McConville W F, Lammert P E, Schiffer P and Crespi V H 2007 *Phys. Rev. Lett.* **98** 217203

[44] Ke X, Li J, Nisoli C, Lammert P E, McConville W, Wang R F, Crespi V H and Schiffer P 2008 *Phys. Rev. Lett.* **101** 037205

[45] Schumann A, Sothmann B, Szary P and Zabel H 2010 *Appl. Phys. Lett.* **97** 022509

[46] Farhan A, Derlet P M, Kleibert A, Balan A, Chopdekar R V, Wyss M, Anghinolfi L, Nolting F and Heyderman L J 2013 *Nat. Phys.* **9** 375–382

[47] Farhan A, Derlet P M, Kleibert A, Balan A, Chopdekar R V, Wyss M, Perron J, Scholl A, Nolting F and Heyderman L J 2013 *Phys. Rev. Lett.* **111** 057204

[48] Porro J M, Bedoya-Pinto A, Berger A and Vavassori P 2013 *New J. Phys.* **15** 055012

[49] Drisko J, Daunheimer S and Cumings J 2015 *Phys. Rev. B* **91** 224406

[50] Zografos O, Soree B, Vaysset A, Cosemans S, Amaru L, Gaillardon P E, De Micheli G, Lauwereins R, Sayan S, Raghavan P, Radu I P and Thean A 2015 Design and benchmarking of hybrid CMOS-Spin Wave Device Circuits compared to 10nm CMOS *2015 IEEE 15th International Conference on Nanotechnology (IEEE-NANO)* (IEEE) pp 686–689

[51] Csaba G, Papp Á and Porod W 2017 *Phys. Lett. A* **381** 1471–1476

[52] Le B L, Rench D W, Misra R and O'Brien L 2015 *New Journal of ...* **17** 023047

[53] Branford W R, Ladak S, Read D E, Zeissler K and Cohen L F 2012 *Science* **335** 1597–1600

[54] Le B L, Park J, Sklenar J, Chern G W, Nisoli C, Watts J D, Manno M, Rench D W, Samarth N, Leighton C and Schiffer P 2017 *Phys. Rev. B* **95** 060405

[55] Park J, Le B L, Sklenar J, Chern G W, Watts J D and Schiffer P 2017 *Phys. Rev. B* **96** 024436

[56] Jungfleisch, M B, Zhang, W, Winkler, R and Hoffmann, A 2017 *Spin-Orbit Torques and Spin Dynamics* (*In: Dyakonov M. (eds) Spin Physics in Semiconductors, Springer Series in Solid-State Sciences, vol 157* vol 157) (Springer, Cham)

[57] Kruglyak V V, Demokritov S O and Grundler D 2010 *J. Phys. D: Appl. Phys.* **43** 264001

[58] Krawczyk M and Grundler D 2014 *J. Phys.: Condens. Matter* **26** 123202–33

[59] Bailleul M, Olligs D and Fermon C 2003 *Phys. Rev. Lett.* **91** 137204

[60] Jorzick J, Demokritov S O, Hillebrands B, Bailleul M, Fermon C, Guslienko K Y, Slavin A N, Berkov D V and Gorn N L 2002 *Phys. Rev. Lett.* **88** 047204

[61] Park J P, Eames P, Engebretson D M, Berezovsky J and Crowell P A 2002 *Phys. Rev. Lett.* **89** 277201

[62] Kostylev M, Schrader P, Stamps R L, Gubbiotti G, Carlotti G, Adeyeye A O, Goolaup S and Singh N 2008 *Appl. Phys. Lett.* **92** 132504–4

[63] Tacchi S, Madami M, Gubbiotti G, Carlotti G, Adeyeye A O, Neusser S, Botters B and Grundler D 2010 *IEEE Trans. Magn.* **46** 172–178

[64] Ulrichs H, Lenk B and Münzenberg M 2010 *Appl. Phys. Lett.* **97** 092506

[65] Neusser S, Botters B, Becherer M, Schmitt-Landsiedel D and Grundler D 2008 *Appl. Phys. Lett.* **93** 122501

[66] Ding J, Tripathy D and Adeyeye A O 2011 *J. Appl. Phys.* **109** 07D304

[67] Ding J, Tripathy D and Adeyeye A O 2012 *EPL (Europhysics Letters)* **98** 16004

[68] Gubbiotti G, Zhou X, Haghshenasfard Z, Cottam M G and Adeyeye A O 2018 *Phys. Rev. B* **97** 134428

[69] Zhou X, Chua G L, Singh N and Adeyeye A O 2016 *Adv. Funct. Mater.* **26** 1437–1444

[70] Gilbert I, Chern G W, Zhang S, O'Brien L, Fore B, Nisoli C and Schiffer P 2014 *Nat. Phys.* **10** 670–675

[71] Phatak C, Petford-Long A K, Heinonen O,

Tanase M and De Graef M 2011 *Phys. Rev. B* **83** 174431

[72] Sklenar J, Bhat V S, DeLong L E and Ketterson J B 2013 *J. Appl. Phys.* **113** 17B530

[73] Brajuskovic V, Barrows F, Phatak C and Petford-Long A K 2016 *Sci. Rep.* **6** 34384

[74] de Araujo C I L, Silva R C, Ribeiro I R B, Nascimento F S, Felix J F, Ferreira S O, Mól L A S, Moura-Melo W A and Pereira A R 2014 *Applied Physics Letters* **104** 092402

[75] Ribeiro I R B, Felix J F, Figueiredo L C, Morais P C, Ferreira S O, Moura-Melo W A, Pereira A R, Quindeau A and de Araujo C I L 2016 *Journal of Physics: Condensed Matter* **28** 456002

[76] McGuire T and Potter R 1975 *IEEE Trans. Magn.* **11** 1018–1038

[77] Nakayama H, Althammer M, Chen Y T, Uchida K, Kajiwara Y, Kikuchi D, Ohtani T, Geprägs S, Opel M, Takahashi S, Gross R, Bauer G E W, Goennenwein S T B and Saitoh E 2013 *Phys. Rev. Lett.* **110** 206601

[78] Tsymbal E and Pettifor D 2001 Perspectives of Giant Magnetoresistance *Solid State Physics, Vol. 56* ed Ehrenreich H and Spaepen F (Academic Press) pp 113–237 ISBN 9780080865201

[79] Jungfleisch M B, Sklenar J, Ding J, Park J, Pearson J E, Novosad V, Schiffer P and Hoffmann A 2017 *Phys. Rev. Appl.* **8** 064026 (*Preprint* 1710.10534)

[80] Hoffmann A 2013 *IEEE Trans. Magn.* **49** 5172–5193

[81] Jungfleisch M B, Zhang W, Jiang W and Hoffmann A 2015 *SPIN* **05** 1530005

[82] Dyakonov M I and Perel V I 1971 *Sov. JETP Lett.* **13** 467

[83] Liu L, Moriyama T, Ralph D C and Buhrman R A 2011 *Phys. Rev. Lett.* **106** 036601

[84] Kalarickal S S, Krivosik P, Wu M, Patton C E, Schneider M L, Kabos P, Silva T J and Nibarger J P 2006 *J. Appl. Phys.* **99** 093909

[85] Jungfleisch M B, Zhang W, Iacocca E, Sklenar J, Ding J, Jiang W, Zhang S, Pearson J E, Novosad V, Ketterson J B, Heinonen O and Hoffmann A 2016 *Phys. Rev. B* **93** 100401 (*Preprint* 1601.01219)

[86] Montoncello F, Giovannini L, Bang W, Ketterson J B, Jungfleisch M B, Hoffmann A, Farmer B W and De Long L E 2018 *Phys. Rev. B* **97** 014421

[87] Bang W, Jungfleisch M B, Montoncello F, Farmer B W, Lapa P N, Hoffmann A, Giovannini L, De Long L E and Ketterson J B 2017 *AIP Adv.* **8** 056020

[88] Bang W, Montoncello F, Jungfleisch M B, Hoffmann A, Giovannini L and Ketterson J B 2019 *Phys. Rev. B* **99** 014415

[89] Bhat V S, Heimbach F, Stasinopoulos I and Grundler D 2016 *Phys. Rev. B* **93** 140401

[90] Liu L, Pai C F, Li Y, Tseng H W, Ralph D C and Buhrman R A 2012 *Science* **336** 555–558

[91] Rippard W, Pufall M, Kaka S, Russek S and Silva T 2004 *Phys. Rev. Lett.* **92** 027201

[92] Demidov V E, Urazhdin S, Zholud A, Sadovnikov A V and Demokritov S O 2014 *Appl. Phys. Lett.* **105** 172410

[93] Mohseni S M, Sani S R, Persson J, Nguyen T N A, Chung S, Pogoryelov Y, Muduli P K, Iacocca E, Eklund A, Dumas R K, Bonetti S, Deac A, Hoefer M A and Akerman J 2013 *Science* **339** 1295–1298

[94] Kiselev S I, Sankey J C, Krivorotov I N, Emley N C, Schoelkopf R J, Buhrman R A and Ralph D C 2003 *Nature* **425** 380–383

[95] Tsoi M, Jansen A G M, Bass J, Chiang W C, Tsoi V and Wyder P 2000 *Nature* **406** 46–48

[96] Schönhense G 2004 *J. Electron Spectros. Relat. Phenomena* **137-140** 769–783

[97] Schneider C M, Krasyuk A, Nepijko S, Oelsner A and Schönhense G 2006 *J. Magn. Magn. Mater.* **304** 6–9

[98] Fischer P 2010 *Mater. Today* **13** 14–22

[99] Tonner B, Dunham D, Droubay T, Kikuma J, Denlinger J, Rotenberg E and Warwick A 1995 *J. Electron Spectros. Relat. Phenomena* **75** 309–332

[100] Anders S, Padmore H A, Duarte R M, Renner T, Stammler T, Scholl A, Scheinfein M R, Stöhr J, Séve L and Sinkovic B 1999 *Rev. Sci. Instrum.* **70** 3973–3981

[101] Hermsmeier B, Stöhr J, Wu Y, Samant M, Harp G, Koranda S, Dunham D and Tonner B P 1994 *J. Appl. Phys.* **75** 6890–6890

[102] Farhan A, Saccone M, Petersen C F, Dhuey S, Chopdekar R V, Huang Y L, Kent N, Chen Z, Alava M J, Lippert T, Scholl A and van Dijken S 2019 *Sci. Adv.* **5** eaav6380

[103] Rhensius J, Heyne L, Backes D, Krzyk S, Heyderman L J, Joly L, Nolting F and Kläui M 2010 *Phys. Rev. Lett.* **104** 067201

[104] Uhlíř V, Pizzini S, Rougemaille N, Novotný J, Cros V, Jiménez E, Faini G, Heyne L, Sirotti F,

Tieg C, Bendounan A, Maccherozzi F, Belkhou R, Grollier J, Anane A and Vogel J 2010 *Phys. Rev. B* **81** 224418

[105] Stein F U, Bocklage L, Weigand M and Meier G 2013 *Sci. Rep.* **3** 1737

[106] Choe S B, Acremann Y, Scholl A, Bauer A, Doran A, Stöhr J and Padmore H A 2004 *Science* **304** 420–2

[107] Curcic M, Van Waeyenberge B, Vansteenkiste A, Weigand M, Sackmann V, Stoll H, Fähnle M, Tyliszczak T, Woltersdorf G, Back C H and Schütz G 2008 *Phys. Rev. Lett.* **101** 197204

[108] Wintz S, Tiberkevich V, Weigand M, Raabe J, Lindner J, Erbe A, Slavin A and Fassbender J 2016 *Nat. Nanotechnol.* **11** 948–953

[109] Foerster M, Macià F, Statuto N, Finizio S, Hernández-Mínguez A, Lendínez S, Santos P V, Fontcuberta J, Hernàndez J M, Kläui M and Aballe L 2017 *Nat. Commun.* **8** 407

[110] Imada S, Sekiyama A and Suga S 2007 *J. Phys. Condens. Matter* **19** 125204

[111] Locatelli A and Bauer E 2008 *J. Phys. Condens. Matter* **20** 093002

[112] Cheng X M and Keavney D J 2012 *Reports Prog. Phys.* **75** 026501

[113] Stoll H, Noske M, Weigand M, Richter K, Krüger B, Reeve R M, Hänze M, Adolff C F, Stein F U, Meier G, Kläui M and Schütz G 2015 *Front. Phys.* **3** 26

[114] Zeissler K, Walton S K, Ladak S, Read D E, Tyliszczak T, Cohen L F and Branford W R 2013 *Sci. Rep.* **3** 1252

[115] Weigand M, Van Waeyenberge B, Vansteenkiste A, Curcic M, Sackmann V, Stoll H, Tyliszczak T, Kaznatcheev K, Bertwistle D, Woltersdorf G, Back C H and Schütz G 2009 *Phys. Rev. Lett.* **102** 077201

[116] Backes D, Macià F, Bonetti S, Kukreja R, Ohldag H and Kent A 2015 *Phys. Rev. Lett.* **115** 127205

[117] Behncke C, Adolff C F, Wintz S, Hänze M, Schulte B, Weigand M, Finizio S, Raabe J and Meier G 2018 *Sci. Rep.* **8** 186

[118] Sluka V, Schneider T, Gallardo R A, Kákay A, Weigand M, Warnatz T, Mattheis R, Roldán-Molina A, Landeros P, Tiberkevich V, Slavin A, Schütz G, Erbe A, Deac A, Lindner J, Raabe J, Fassbender J and Wintz S 2019 *Nat. Nanotechnol.* **14** 328–333

[119] Bonetti S 2017 *J. Phys. Condens. Matter* **29** 133004

[120] Sebastian T, Schultheiss K, Obry B, Hillebrands B and Schultheiss H 2015 *Front. Phys.* **3** 1589

[121] Donahue M and Porter D 1999 OOMMF User's Guide, Version 1.0 Interagency Report NISTIR 6376 Tech. rep. National Institute of Standards and Technology Gaithersburg, MD

[122] Vansteenkiste A, Leliaert J, Dvornik M, Helsen M, Garcia-Sanchez F and Van Waeyenberge B 2014 *AIP Adv.* **4** 107133

[123] Mamica S, Zhou X, Adeyeye A, Krawczyk M and Gubbiotti G 2018 *Phys. Rev. B* **98** 054405

[124] Bhat V S, Sklenar J, Farmer B, Woods J, Hastings J T, Lee S J, Ketterson J B and De Long L E 2013 *Phys. Rev. Lett.* **111** 077201

[125] Li Y, Gubbiotti G, Casoli F, Gonçalves F J T, Morley S A, Rosamond M C, Linfield E H, Marrows C H, McVitie S and Stamps R L 2017 *J. Phys. D. Appl. Phys.* **50** 015003

[126] Grundler D *Private communication.*

[127] Bhat V S, Heimbach F, Stasinopoulos I and Grundler D 2017 *Phys. Rev. B* **96** 014426

[128] Jungfleisch M B, Zhang W, Ding J, Jiang W, Sklenar J, Pearson J E, Ketterson J B and Hoffmann A 2016 *Appl. Phys. Lett.* **108** 052403

[129] Cowburn R P, Koltsov D K, Adeyeye A O and Welland M E 1999 *Phys. Rev. Lett.* **83** 1042–1045

[130] Novosad V, Guslienko K Y, Shima H, Otani Y, Fukamichi K, Kikuchi N, Kitakami O and Shimada Y 2001 *IEEE Trans. Magn.* **37** 2088–2090

[131] Guslienko K Y, Novosad V, Otani Y, Shima H and Fukamichi K 2001 *Appl. Phys. Lett.* **78** 3848–3850

[132] Metlov K L and Guslienko K Y 2002 *J. Magn. Magn. Mater.* **242-245** 1015–1017

[133] Shinjo T, Okuno T, Hassdorf R, Shigeto K and Ono T 2000 *Science* **289** 930–932

[134] Schneider M, Hoffmann H and Zweck J 2000 *Appl. Phys. Lett.* **77** 2909–2911

[135] Miltat J and Thiaville A 2002 *Science* **298**

[136] Wachowiak A, Wiebe J, Bode M, Pietzsch O, Morgenstern M and Wiesendanger R 2002 *Science* **298** 577–80

[137] Guslienko K Y, Ivanov B A, Novosad V, Otani Y, Shima H and Fukamichi K 2002 *J. Appl. Phys.* **91** 8037–8039

[138] Park J P, Eames P, Engebretson D M, Berezovsky J and Crowell P A 2003 *Phys. Rev. B* **67** 020403

[139] Pribiag V S, Krivorotov I N, Fuchs G D,

Braganca P M, Ozatay O, Sankey J C, Ralph D C and Buhrman R A 2007 *Nat. Phys.* **3** 498–503

[140] Van Waeyenberge B, Puzic A, Stoll H, Chou K W, Tyliszczak T, Hertel R, Fähnle M, Brückl H, Rott K, Reiss G, Neudecker I, Weiss D, Back C H and Schütz G 2006 *Nature* **444** 461–4

[141] Xiao Q F, Rudge J, Choi B C, Hong Y K and Donohoe G 2006 *Appl. Phys. Lett.* **89** 262507

[142] Liu Y, Gliga S, Hertel R and Schneider C M 2007 *Appl. Phys. Lett.* **91** 112501

[143] Wang H L, Du C H, Pu Y, Adur R, Hammel P C and Yang F Y 2014 *Phys. Rev. Lett.* **112** 197201

[144] Kelly O d, Anane A, Bernard R, Ben Youssef J, Hahn C, Molpeceres A H, Carrétéro C, Jacquet E, Deranlot C, Bortolotti P, Lebourgeois R, Mage J C, de Loubens G, Klein O, Cros V and Fert A 2013 *Appl. Phys. Lett.* **103** 082408

[145] Papaioannou E T, Fuhrmann P, Jungfleisch M B, Brächer T, Pirro P, Lauer V, Lösch J and Hillebrands B 2013 *Appl. Phys. Lett.* **103** 162401

[146] Demidov V E, Urazhdin S, Ulrichs H, Tiberkevich V, Slavin A, Baither D, Schmitz G and Demokritov S O 2012 *Nat. Mater.* **11** 1028–1031

[147] Cornelissen L J, Liu J, Duine R A, Ben Youssef J and van Wees B J 2015 *Nat. Phys.* **11** 1022–1026

[148] Zhang W, Jungfleisch M B, Jiang W, Pearson J E, Hoffmann A, Freimuth F and Mokrousov Y 2014 *Phys. Rev. Lett.* **113** 196602

[149] Chern G W 2017 *Phys. Rev. Appl.* **8** 064006

[150] Luo Z, Dao T P, Hrabec A, Vijayakumar J, Kleibert A, Baumgartner M, Kirk E, Cui J, Savchenko T, Krishnaswamy G, Heyderman L J and Gambardella P 2019 *Science* **363** 1435–1439

[151] Jungfleisch M B, Ding J, Zhang W, Jiang W, Pearson J E, Novosad V and Hoffmann A 2017 *Nano Letters* **17** 8–14

[152] Wu F Y 1982 *Reviews of Modern Physics* **54** 235

[153] Arava H, Leo N, Schildknecht D, Cui J, Vijayakumar J, Derlet P, Kleibert A and Heyderman L 2018 *arXiv.org:1903.01887* (*Preprint* `1812.06936`)

[154] Arava H, Derlet P M, Vijayakumar J, Cui J, Bingham N S, Kleibert A and Heyderman L J 2018 *Nanotechnology* **29** 265205

[155] Gypens P, Leliaert J and Van Waeyenberge B 2018 *Phys. Rev. Appl* **9** 034004

[156] Grollier J, Querlioz D and Stiles M D 2016 *Proc. IEEE* **104** 2024–2039